J. Fluid Mech. (1999), *vol.* 380, *pp.* 81–116. Printed in the United Kingdom

Sound generation by shock–vortex interactions

By OSAMU INOUE AND YUJI HATTORI

Institute of Fluid Science, Tohoku University, Sendai 980-8577, Japan

(Received 14 April 1997 and in revised form 7 August 1998)

Two-dimensional, unsteady, compressible flow fields produced by the interactions between a single vortex or a pair of vortices and a shock wave are simulated numerically. The Navier–Stokes equations are solved by a finite difference method. The sixth-order-accurate compact Padé scheme is used for spatial derivatives, together with the fourth-order-accurate Runge–Kutta scheme for time integration. The detailed mechanics of the flow fields at an early stage of the interactions and the basic nature of the near-field sound generated by the interactions are studied. The results for both a single vortex and a pair of vortices suggest that the generation and the nature of sounds are closely related to the generation of reflected shock waves. The flow field differs significantly when the pair of vortices moves in the same direction as the shock wave than when opposite to it.

1. Introduction

Attention has been given to the interaction between shock waves and vortices because vortices are building blocks of supersonic turbulent flows. The interaction of shock waves with turbulent flows is known to be one of the major sources of noise, and so closely related to a variety of aerodynamic problems such as the noise produced by rockets, high-speed aircraft and helicopters (Ribner 1954, 1955, 1981, 1985; Tam 1995; McCroskey 1995). A number of studies have been performed experimentally (Hollingsworth & Richards 1955; Dosanjh & Weeks 1965), theoretically (Lighthill 1953; Hollingsworth & Richards 1956; Weeks & Dosanjh 1967; Ting 1974; Ribner 1985), and computationally (Pao & Salas 1981; Bayliss & Maestrello 1981; Zang, Hussaini & Bushnell 1984; Meadows, Kumar & Hussaini 1991), among others.

Hollingsworth & Richards (1955) showed experimentally that when a columnar vortex passes through a planar shock wave, a cylindrical acoustic wave appears with a portion cut off by the shock wave. They observed that the acoustic wave consists of alternating compressions and rarefactions. Later, Hollingsworth & Richards (1956) predicted by linearized analyses that the acoustic wave is composed of four alternating compression and rarefaction regions (quadrupolar nature). Using a spark schlieren and Mach–Zehnder interferometer, Dosanjh & Weeks (1965) measured experimentally the circumferential distribution of pressure of the acoustic wave and verified the prediction of Hollingsworth & Richards. These experimental results of Hollingsworth & Richards (1955) and Dosanjh & Weeks (1965) were obtained for the interaction of a shock wave with a single, two-dimensional vortex.

Using a shadowgraph technique, Minota (1993) studied experimentally the interaction of a spherical shock wave with a vortex ring, which were moving in opposite directions. She observed the complex structure of the shock wave distortion: diffraction, refraction, branching and focusing. Though direct information on the acoustic sound generated by the interaction was not provided, the mechanism of the shock

wave–vortex ring interaction observed by Minota may be closely related to the sound generation. Similar experimental results for a shock wave–vortex ring interaction have also been reported by Szumowski & Sobieraj (1996).

Both experiments (Naumann & Hermanns 1973; Minota 1993) and computations (Ellzey *et al.* 1995; Guichard, Vervisch & Domingo 1995) show that an initially planar shock wave deforms significantly through the interaction with a vortex. This deformation is also implicit in a successful linear theory (Ribner 1985), and has been explicitly calculated by Filotas (1967). Some other linear theories (Hollingsworth & Richards 1956; Weeks & Dosanjh 1967; Ting 1974) assume that the distortion of the shock wave is negligibly small.

Direct numerical simulations of the far-field sound have become feasible in recent years (Lee, Lele & Moin 1993; Colonius, Lele & Moin 1994; Mitchell, Lele & Moin 1995). In these simulations, the Navier–Stokes equations were solved by a finite difference method. In order to precisely capture the far-field sound, the sixth-order-accurate compact Padé scheme (Lele 1992) was used for spatial derivatives, together with the third-/fourth-order-accurate Runge–Kutta scheme for time integration. Also, the computational domains extended to cover the acoustic far field, using stretched meshes. For the case of the interaction of a shock wave with vortices, fine meshes must be concentrated near the shock wave in order to describe adequately the shock structure. Thus, the direct simulation of the far-field sound requires much finer resolution, and thus many more grid points, than for the cases without shock waves, resulting in an increase in the memory storage and computation time; even with the use of stretched meshes, the simulation is often limited to the near field.

Guichard *et al.* (1995) studied the flow field in a mixing zone produced by the interaction between a single vortex or a pair of vortices and a shock wave of Mach number 1.2. They solved the unsteady compressible Navier–Stokes equations using a sixth-order Padé spatial discretization and a third-order-accurate Runge–Kutta method for time-integration. Their results showed the distortion of the shock wave and the formation of triple points through the interaction. They also showed that the patterns of the shock wave distortion are affected by the self-induced translational motion of the vortex pair with respect to the shock wave. Little information on the sound generation was provided except for the shock wave distortion. Ellzey *et al.* (1995) studied the interaction between a shock wave and a single vortex. The unsteady compressible Euler equations were solved by a fourth-order-accurate finite difference algorithm (the flux-corrected transport algorithm). They examined the effects of strengths of both a shock wave and a vortex, and showed that for the case of a strong shock wave the transmitted shock structure results in a Mach reflection while for the case of a weak shock wave it is a regular reflection. They also showed that through the interaction the precursor wave appears first, and then the second acoustic wave follows. Both waves showed a quadrupolar nature. Meadows & Caughey (1996) studied the flow field generated by the interaction between a shock wave and a vortex ring. The axisymmetric Euler equations were solved by a third-order-accurate shock-capturing scheme (ENO scheme). They observed that the shock wave is deformed by the interaction and that the shock deformation leads to the generation of acoustic waves and contact surfaces.

The purpose of this paper is to study, using direct Navier–Stokes simulations, the detailed mechanics of the flow field produced by the interactions between a single vortex or a pair of vortices and a shock wave, and to increase our understanding of the near-field sound generated by the interactions. First, we examine the basic nature of the sound pressure field for the case of a single vortex, which is one of the most simplified models of shock–turbulent flow interaction. We also simulate a flow with

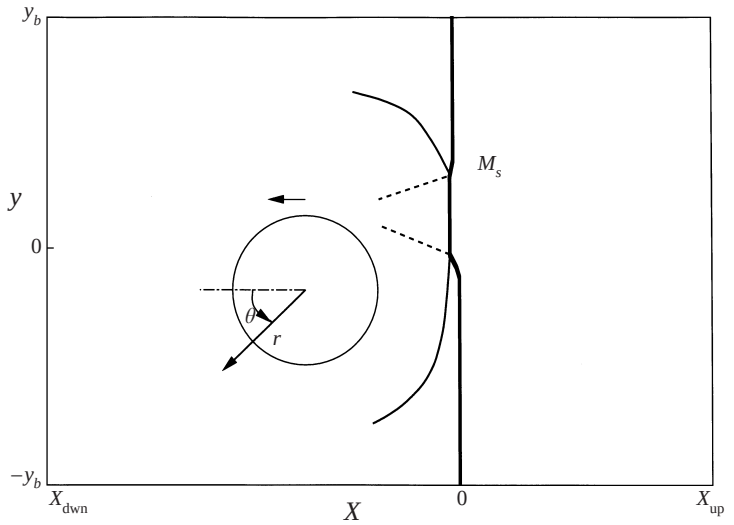

FIGURE 1. Schematic diagram of the flow model.

the same shock and vortex Mach numbers as those in the experiments of Dosanjh & Weeks (1965) and compare the result with the experimental results and the theoretical results of Ribner (1985) and the inviscid computational results of Ellzey *et al.* (1995). We then examine the basic nature of the sound pressure field for the case of a pair of vortices, as an example of a somewhat more complex flow field. Based on the results for a single vortex, we will discuss the results for a vortex pair. The effects of the strengths of both shock waves and vortices are also examined.

2. Mathematical formulation and numerical procedure

A schematic diagram of flow model is presented in figure 1. We adopt a coordinate system which moves with the shock wave. The computational domain is prescribed to be rectangular ($x_{\text{dwn}} \leqslant x \leqslant x_{\text{up}}, -y_b \leqslant y \leqslant y_b$), and the shock wave is assumed to be fixed at $x = 0$. In this study, the length scale is non-dimensionalized by the core radius R of the vortex. Vortices are located initially at (x_v, y_v) with $y_v = 0$ for a single vortex and at $(x_v, \pm y_v)$ for a pair of vortices. The vortices move from right to left with respect to the shock wave.

The two-dimensional, compressible Navier–Stokes equations are solved by a finite difference method. For spatial derivatives, a sixth-order-accurate compact Padé scheme (third-order accurate at the boundaries) proposed by Lele (1992) is adopted. The fourth-order Runge–Kutta scheme is used for time-integration. Non-reflecting boundary conditions (Poinsot & Lele 1992) are used at $x = x_{\text{dwn}}$ for the subsonic outflow. The flow quantities at the supersonic inlet ($x = x_{\text{up}}$) are fixed. Periodic boundary conditions are imposed at $y = \pm y_b$. A non-uniform mesh system is applied in this study and, following the suggestion of Lele (1992), more than seven points are distributed within the shock wave in order to precisely capture it.

For the case of the interaction of a shock wave with a single vortex, the vortex is assumed to have the following velocity distributions initially (Taylor 1918):

$$\text{tangential velocity: } u_\theta(r) = M_v r \exp[(1 - r^2)/2],$$
$$\text{radial velocity: } u_r = 0.$$

Therefore, the vorticity distribution is given by

$$\omega(r) = M_v(2 - r^2)\exp[(1 - r^2)/2].$$

In the above expressions, the velocity components are normalized by the sound velocity a_∞ upstream of the shock wave. The Mach number M_v of the vortex is defined by $M_v = u_{\theta\max}/a_\infty$, where $u_{\theta\max}$ is the maximum tangential velocity. The following conditions are assumed for the initial distributions of the pressure and the density:

$$p/\rho^\gamma = \text{constant},$$

$$\mathrm{d}p/\mathrm{d}r = \rho u_\theta^2/r.$$

As a result, the pressure distribution is expressed by

$$p(r) = \frac{1}{\gamma}\left[1 - \frac{\gamma - 1}{2}M_v^2\exp(1 - r^2)\right]^{\gamma/(\gamma-1)},$$

$$\rho(r) = \left[1 - \frac{\gamma - 1}{2}M_v^2\exp(1 - r^2)\right]^{1/(\gamma-1)}.$$

Here the density ρ and the pressure p are normalized by ρ_∞ and the sound velocity a_∞, where the subscript ∞ denotes the quantity upstream of the shock wave. The symbol γ denotes the ratio of specific heats and is fixed to be 1.4. The initial distributions of flow quantities around the vortex are presented in figure 2 for $M_v = 0.25$ (solid line) and 0.5 (dashed line). It should be noted that the total circulation of this vortex is zero and, as seen from figure 2, the effect of the vortex is negligibly small beyond $r = 4$. This vortex is adopted in this study such that the fixed upstream boundary conditions at $x = x_{\text{up}}$ as well as the periodic boundary conditions at $y = \pm y_b$ are guaranteed in a finite computational domain. A similar vortex with zero total circulation had been adopted by Ellzey *et al.* (1995). The initial flow field prescribed above is not an exact solution of the Navier–Stokes equations. However, the acoustic transients associated with the initial condition were found to be negligibly small compared with the sound pressure field produced by the shock–vortex interaction.

For the case of the interaction with a pair of vortices, each vortex is assumed to have the same nature as above except for the sense of rotation, and the initial flow field is prescribed by the superposition of the flow fields produced by each single vortex.

In this study, the computational domain is prescribed as follows:

upstream boundary: $x_{\text{up}} = 8.0$,
downstream boundary: $x_{\text{dwn}} = -20.0$,
upper and lower boundaries: $\pm y_b = \pm 12.0$,
initial locations of vortices: $x_v = 2.0, y_v = 0$ for a single vortex,
$x_v = 2.0, y_v = 2.0$ for a pair of vortices.

As noted before, the effect of the vortex is negligibly small beyond $r = 4$. Therefore, for the case in which the initial distance between the two vortices is larger than 8, the vortices may not behave as a pair; the prescribed initial distance between the two vortices may be considered as a moderate choice.

The number of grid points is 1044 (x-direction)×1170 (y-direction). The spacing near the shock wave $(\Delta x_s, \Delta y_s)$ is $\Delta x_s/R = 0.0025$ and $\Delta y_s/R = 0.0025$, while the

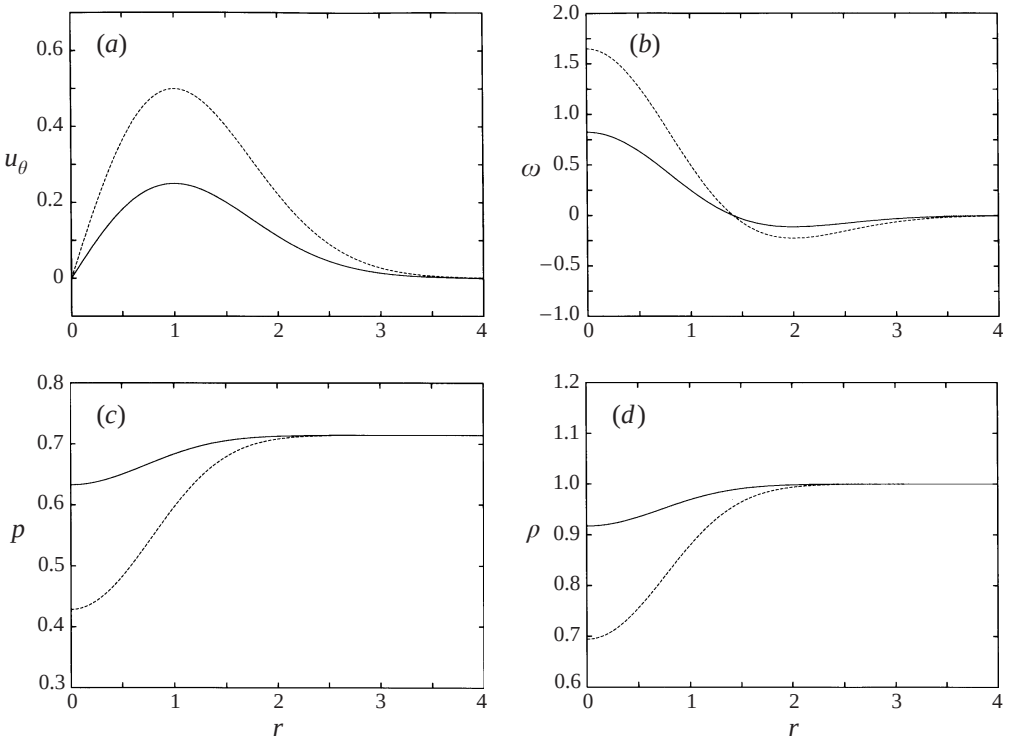

FIGURE 2. Initial distributions of flow quantities around a vortex for $M_v = 0.25$ (solid line) and $M_v = 0.5$ (dashed line). (*a*) Tangential velocity U_θ, (*b*) vorticity ω, (*c*) pressure p, (*d*) density ρ.

	M_s	M_v	Re
Case A	1.2	0.5	400
B	1.2	0.25	400
C	1.2	0.25	800
D	1.05	0.5	400
E	1.05	0.25	400
F	1.05	0.25	800
G	1.29	0.39	800

TABLE 1. Parameters of shock wave and vortices used for the simulations.

spacing near the boundary $(\Delta x_b, \Delta y_b)$ is $\Delta x_b/R = 0.14$ and $\Delta y_b/R = 0.07$. The time step is $\Delta t/(R/a_\infty) = 1.75 \times 10^{-4}$. The numerical accuracy for these spatial and temporal resolutions has been confirmed and typical results for the numerical tests will be presented in the following section (figures 9 and 10).

The Mach number of a shock wave (M_s), defined by $M_s = u_\infty/a_\infty$, is prescribed to be either 1.05 or 1.2. As will be seen later, through the interaction with the vortices the shock wave shows a Mach reflection when $M_s = 1.2$ and a regular reflection when $M_s = 1.05$. The Mach number of a vortex (M_v) is 0.25 or 0.5. The Reynolds number is defined by $Re = \rho_\infty a_\infty R/\mu_\infty$ and is prescribed to be either 400 or 800. The Prandtl number, Pr, is assumed to be constant with a value of 0.75. The combinations of the parameters used for the simulations are listed in table 1 (Cases A to F).

In addition, a simulation at the same combination of M_s and M_v as that in the experiment of Dosanjh & Weeks (1965) is performed (Case G in table 1). In the experiment, a shock wave passed over an inclined airfoil and created a starting vortex. The shock wave propagated to the end of the shock tube, and, after reflecting, it interacted with the vortex. The shock Mach number was 1.29 and the vortex Mach number was 0.39. The Reynolds number in the experiment was of order 160 000, which is 200 times that in the present simulation, where $Re = 800$.

3. Results for the case of a single vortex

In this section, computational results for the case of shock–single vortex interaction are presented. First, in § 3.1, characteristic features of flow fields and sounds, generated by the interaction, are discussed. It is shown that the generation and nature of the sound waves are related to the deformation and reflection of shock waves. Effects of the shock and vortex Mach numbers and the Reynolds number are also discussed. Then, in § 3.2, the present computational results are compared with experiment, theory and inviscid computational results.

3.1. *Basic structure of sound generation* (*Cases A to F*)

3.1.1. *Evolution of shock–vortex interaction*

A typical example of the time development of the pressure field for the case of a single vortex interacting with a shock wave is presented in figure 3 with $M_s = 1.2, M_v = 0.25$ and $Re = 800$ (Case C). The sound pressure Δp is defined as $\Delta p = (p - p_s)/p_s$ where p_s is the pressure behind the shock wave. The sense of rotation of the vortex is anti-clockwise. In the figure, the symbol $\oplus$ denotes the compression region ($\Delta p > 0$) while $\ominus$ denotes the rarefaction region ($\Delta p < 0$). The shock wave deformation caused by the interaction is schematically presented in figure 4, where time increases from (*a*) to (*c*). As seen from figures 3(*a*) and 4(*a*), immediately after the beginning of the shock wave-vortex interaction, the initially planar shock wave deforms, and a compression region and a rarefaction region appear downstream of the shock wave ($x < 0$). As the interaction develops, the shock wave continues to deform, and a new rarefaction region appears outside the compression region. Simultaneously, a new compression region appears outside the rarefaction region (figure 3*b*). This series of events shows the generation of the precursor (Ribner 1985) and its quadrupolar nature (Hollingsworth & Richards 1955, 1956; Dosanjh & Weeks 1965). The shock wave deforms more and more with the development of the interaction, and eventually reflected shock waves emanate from the compression part of the incident shock wave (figures 3*c* and 4*b*). One of the reflected shock waves (numbered as 1 in figure 4) moves upward while the other one (number 2) moves downward. Due to the anticlockwise rotation of the vortex, the strength of shock wave 1 is larger than that of shock wave 2; the propagation velocity of shock wave 1 is larger than that of shock wave 2. The shock wave reflection is classified as a Mach reflection. The slip lines which emanate from the triple points (denoted by T_1 and T_2) are shown with dashed lines in figure 4(*c*). They are not captured in terms of the pressure in figure 3. Figure 3(*d*) shows that a second acoustic wave also of a quadrupolar nature (hereafter referred to as the second sound) is generated after the precursor, and that the strong compression region of the second sound is behind reflected shock wave 1 and the strong rarefaction region is ahead of shock wave 2.

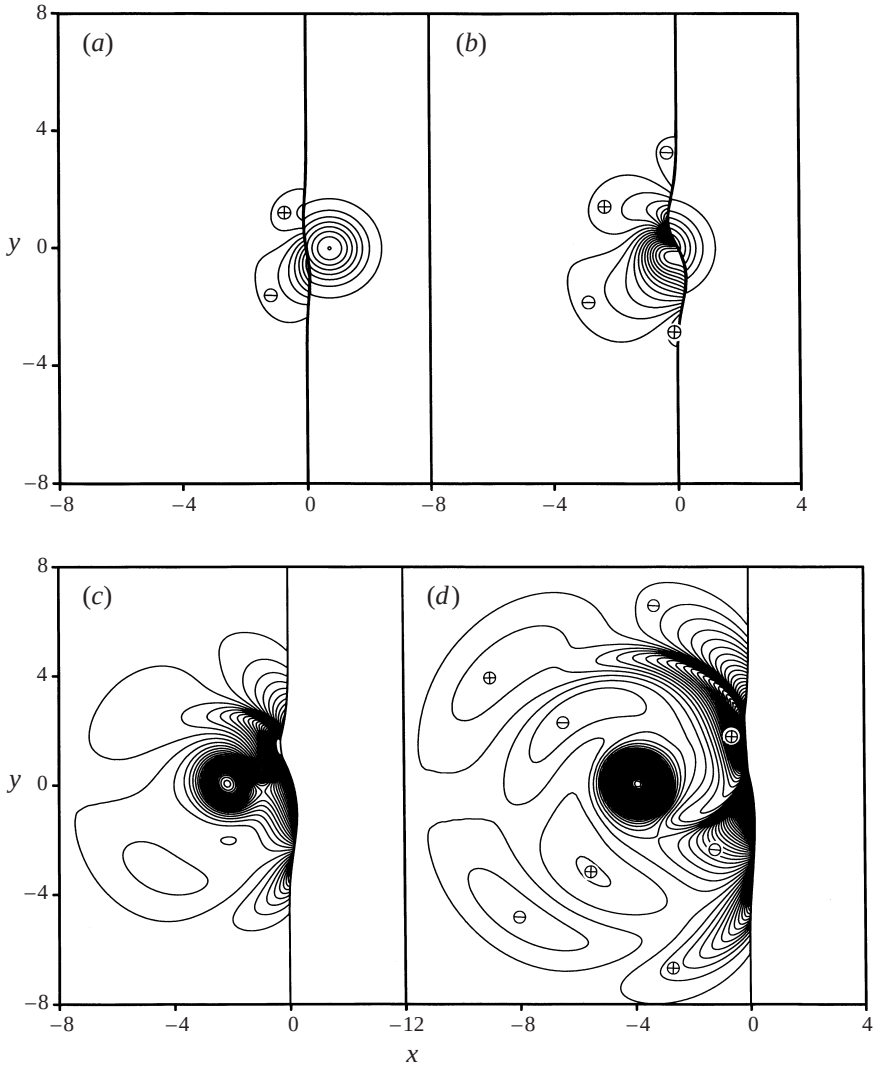

FIGURE 3. Time development of the pressure field (Δp) for the case of a single vortex. Case C. The contour levels are from $\Delta p_{\min} = -0.48$ to $\Delta p_{\max} = 0.16$ with an increment of 0.0108. (*a*) $t = 1.0$, (*b*) $t = 2.0$, (*c*) $t = 4.0$, (*d*) $t = 6.0$.

3.1.2. *Spatial distribution of sound pressure*

In figure 5(*a*) distributions of the sound pressure Δp are plotted against the distance r from the vortex centre for a fixed value of $\theta = -45°$, and in figure 5(*b*) the circumferential variations of Δp of the precursor ($r = 6.0$, solid line) and the second sound ($r = 3.7$, dashed line) at $t = 6.0$ are plotted. (For the coordinates (r, θ), see figure 1.) As seen from figure 5(*a*), both the precursor and the second sound propagate radially from the vortex with time; also the peak values of Δp of both the precursor and the second sound decay with the radial distance r. Figure 5(*b*) shows that the circumferential variation of the sound pressure (quadrupolar nature) of the second sound is opposite in sign to that of the precursor, in agreement with the Euler results of Ellzey *et al.* (1995).

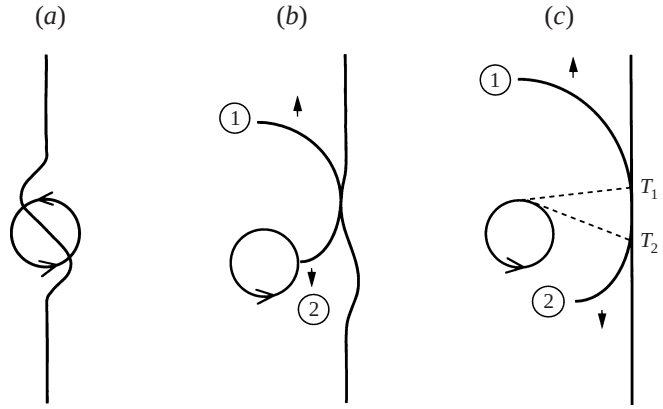

FIGURE 4. Temporal variation of shock wave deformation due to the interaction with a single vortex. Case C. T_1 and T_2 denote the triple points. Time increases from (*a*) to (*c*).

3.1.3. *Sound wave evolution relative to shock wave reflection*

The characteristic nature of the sounds and their relation to the reflected shock waves for the case of a single vortex are schematically shown in figure 6(*a*). Presented in figure 6(*b*) is a shadowgraph of a flow field for Case C, which is obtained from the Laplacian of the density, $\nabla^2\rho$ ($= \partial^2\rho/\partial x^2+\partial^2\rho/\partial y^2$). As was shown in figure 3, through the shock–vortex interaction, the precursor appears first, and then the two reflected shock waves are generated; the precursor is observed ahead of the two reflected shock waves in figure 6(*b*). The sound pressure fields around the two reflected shock waves are different as seen from figure 6(*a*). In the positive *y*-plane, the rarefaction region of the precursor and the compression region of the second sound are respectively located ahead of and behind reflected shock wave 1. On the other hand, in the negative *y*-plane, the rarefaction region of the second sound is ahead of reflected shock wave 2, and the compression region of the precursor is further ahead of the rarefaction region of the second sound; the compression region behind the reflected shock wave 2 is related neither to the precursor nor to the second sound. Here, a question arises: does the compression region behind reflected shock wave 2 have any relation to the sound generation? A clue to the answer lies in the sound pressure field generated by a pair of vortices interacting with a shock wave. As shown later in § 4.2 (for example, figures 17*b* and 20), a similar sound pressure field to that in the negative *y*-plane of figure 6(*a*) is generated when a pair of vortices collides with a shock wave, and there the third sound is generated behind the (merged) reflected shock wave. The third sound generated by the pair of vortices has the same circumferential distribution of Δp as the precursor. This result strongly suggests that in the case of a single vortex, as in the case of the pair of vortices colliding with the shock wave, the third sound may be generated in the course of time and the compression region behind reflected shock wave 2 may form a part of the third sound which has the same quadrupolar nature as the precursor. Unfortunately, the computational domain in this study is not large enough to simulate the entire process of the generation of the third sound for a single vortex; only the compression region of the third sound behind shock wave 2 is captured. (In figure 6(*a*), parentheses denote regions which were not captured in this study but expected to appear at subsequent times.) Confirmation of the generation of the third sound and its circumferential pressure variation is left for future work.

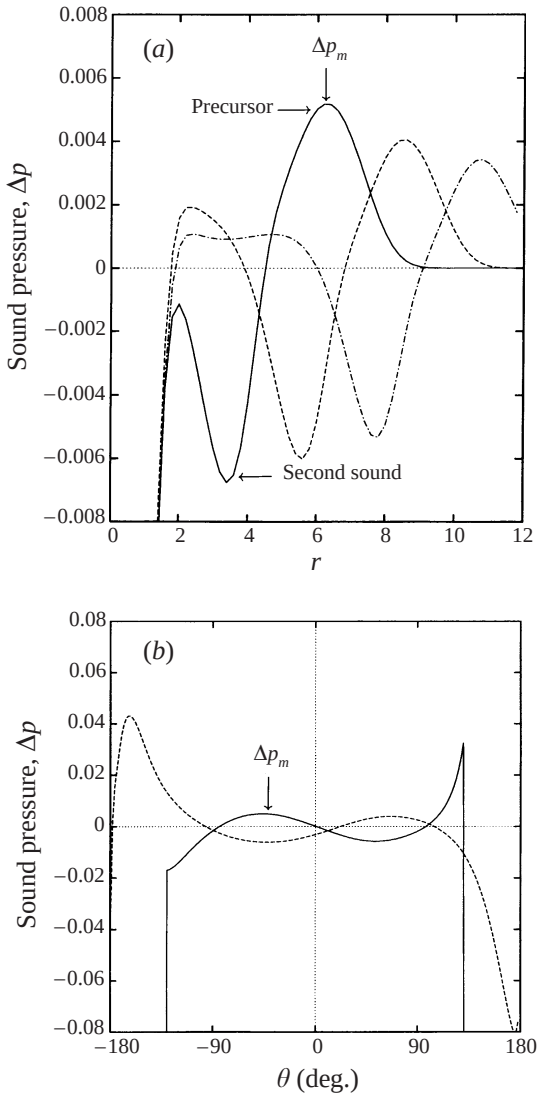

FIGURE 5. Radial and circumferential distributions of the sound pressure Δp. Case C. (*a*) Radial distribution. $\theta = -45°$. ———, $t = 6.0$; — — — —, $t = 8.0$; – · – · –, $t = 10.0$. (*b*) Circumferential distribution. $t = 6.0$. ———, $r = 6.0$ (precursor); — — — —, $r = 3.7$ (second sound).

3.1.4. *Variation with M_s, M_v and Re*

The effects of the parameters (M_s, M_v, Re) on the magnitude of the sound pressure Δp are presented in figure 7, where the peak value of the sound pressure, Δp_m, of the precursor measured at $\theta = -45°$ is plotted. As an example, Δp_m for Case C at $t = 6.0$ is shown by an arrow in figure 5. We can see from figure 7 that the magnitude of the sound pressure generated rises with an increase in M_s as well as in M_v. On the other hand, the effect of Re seems insignificant for the values examined in this study ($Re = 400, 800$), because the Reynolds number is defined based on the core radius of the vortex, which is much larger than the shock wave thickness.

It is known (for example, Landau & Lifshitz 1984) that the decay of the sound pressure in two-dimensional flows is inversely proportional to $r^{1/2}$ in the far field. The

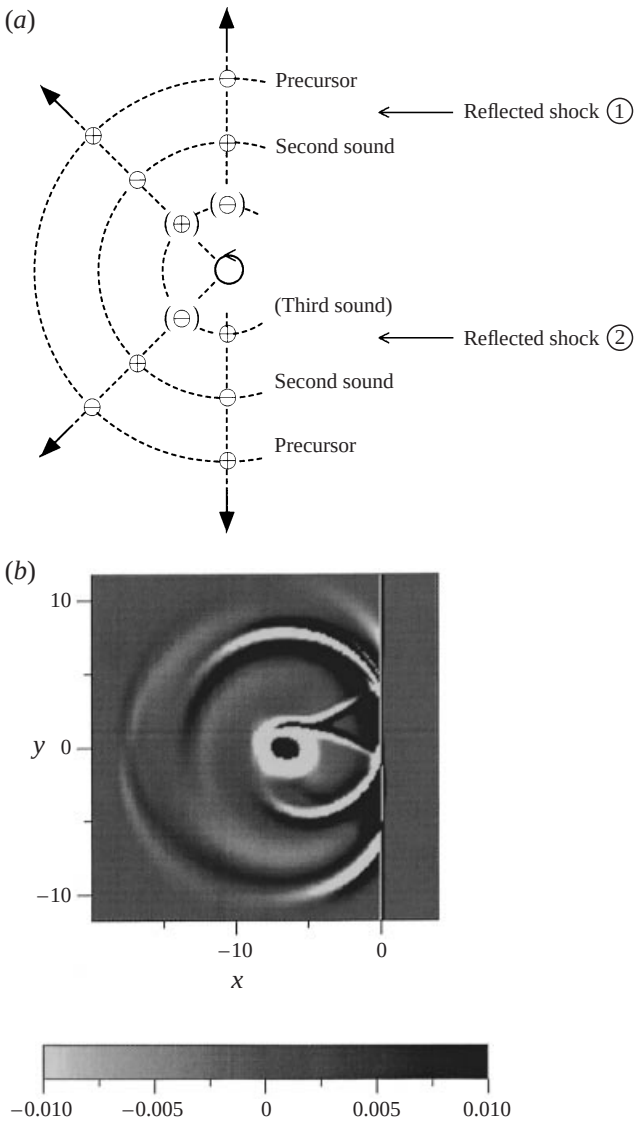

FIGURE 6. Basic nature of sound generation for the case of a single vortex interacting with a shock wave. (*a*) Characteristic nature of the sounds and their relation to the reflected shock waves: ⊕, compression region; ⊖, rarefaction region. Parentheses () denotes the expected region to appear at subsequent times. (*b*) Computational shadowgraph of a flow field for Case C. $t = 9.0$.

computational results in figure 7 have not yet reached the $r^{-1/2}$ line, indicating that the computational domain in this study is not large enough to capture the far-field sound.

Computational shadowgraphs for different combinations of M_s and M_v are presented in figure 8 for $Re = 400$. In all the cases presented, through the shock–vortex interaction, the precursor appears first and then the second sound follows. (As noted before, the third sound was not captured in this study because of the insufficient computational domain and time.) The qualitative features of the two sounds are the same for the six cases examined. By comparing Cases A and B (figures 8*a* and 8*b*)

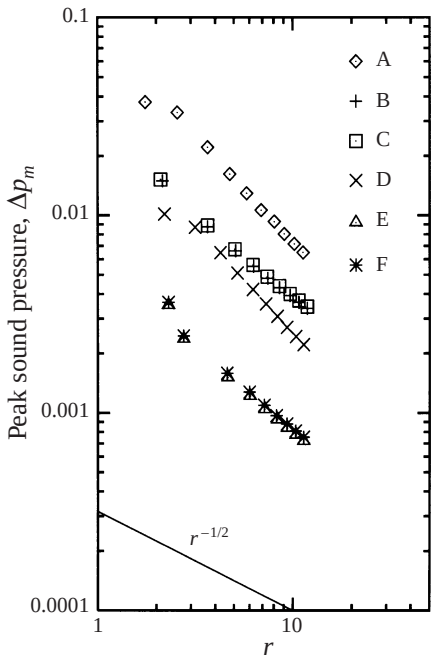

FIGURE 7. Decay of the sound pressure. Symbols: Cases A–F; ———, $\Delta p_m \propto r^{-1/2}$.

with Cases D and E (figures 8*c* and 8*d*), we can see that the shock Mach number M_s determines the type of shock reflection: a Mach reflection for $M_s = 1.2$ and a regular reflection for $M_s = 1.05$. On the other hand, by comparing Case A (figure 8*a*) with Case B (figure 8*b*), or Case D (figure 8*c*) with Case E (figure 8*d*), we can see that the effect of the vortex Mach number M_v appears in the strengths of the reflected shock waves and thus in the magnitude of the sound pressure; a larger M_v leads to stronger compressions and rarefactions.

3.1.5. *Grid refinement study*

As mentioned in the previous section, the spacing near the shock wave $(\Delta x_s, \Delta y_s)$ is prescribed to be $\Delta x_s/R = 0.0025$ and $\Delta y_s/R = 0.0025$. With these spacings, the number of grid points within the shock wave is 43 for $M_s = 1.2$ and 124 for $M_s = 1.05$. The spacing near the boundaries (Δx_b, Δy_b) is prescribed to be $\Delta x_b/R = 0.14$ and $\Delta y_b/R = 0.07$. The time step is 1.75×10^{-4}. In order to examine the reliability of computational results with these resolutions, numerical tests with coarser resolutions were performed. Typical results of the peak sound pressure Δp_m are presented in figure 9, and those of the density field are in figure 10. In figure 9, the prime stands for the results with a coarse resolution. In Case A, M_s and M_v are large while M_s and Re are large in Case C. The spacings of the coarse resolution are $\Delta x_s/R = 0.005$ and $\Delta y_s/R = 0.005, \Delta x_b/R = 0.14$ and $\Delta y_b/R = 0.14$. With these spacings, the number of grid points within the shock wave is 10 for $M_s = 1.2$ and 39 for $M_s = 1.05$. The time step of the coarse resolution is 7.0×10^{-4} in Case A′ and 1.4×10^{-3} in Case C′. As seen from figure 9, the differences of the results between the fine and the coarse resolutions are negligibly small for the peak sound pressure Δp_m. However, the density field for Case A′ in figure 10(*b*) shows that numerical oscillations take place near the

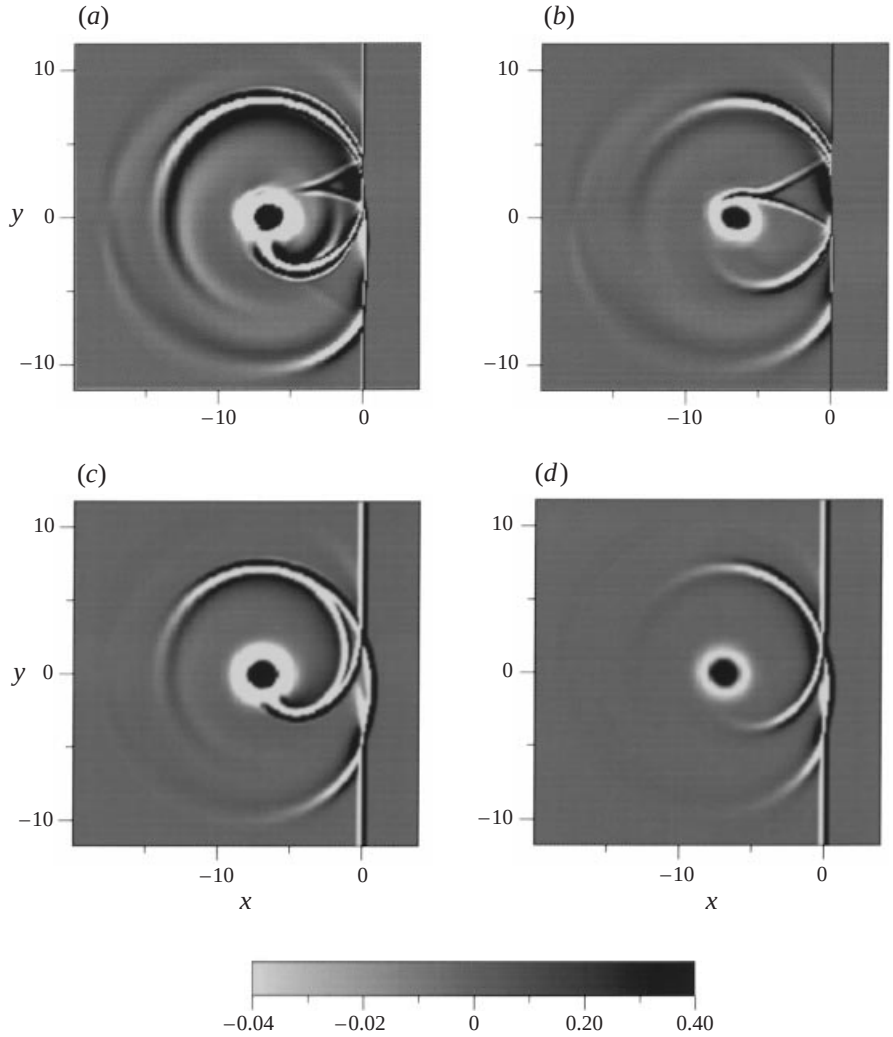

FIGURE 8. Shadowgraphs obtained from $\nabla^2\rho$ for the case of a single vortex. $Re = 400$, $t = 9.0$. (*a*) Case A, (*b*) Case B, (*c*) Case D, (*d*) Case E.

reflected shock waves with the coarse resolution; the fine resolution is adopted in this computation.

3.2. *Comparison with experiment* (*Case G*)

In addition to the calculations described above, a simulation was performed at the same combination of $M_s(= 1.29)$ and $M_v(= 0.39)$ as in the experiment of Dosanjh & Weeks (1965). The Reynolds number in the experiment was of order 160 000, which is 200 times that in the present simulation ($Re = 800$). The present results were also compared to the inviscid Euler simulation by Ellzey *et al.* (1995).

3.2.1. *Overall flow structures*

As a typical example of the flow field, the isopycnics (lines of constant density) and isobars of the sound pressure at $t = 10.3$ are presented in figure 11(*a*) and 11(*b*), respectively. The qualitative features of the flow field are similar to those for $M_s = 1.2$

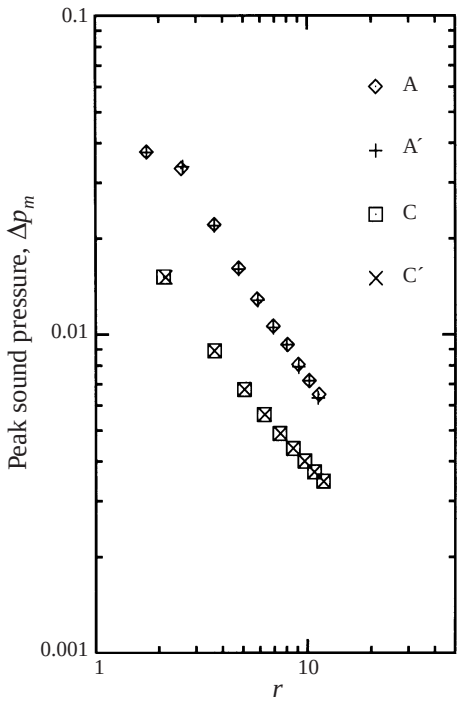

FIGURE 9. Accuracy tests. Decay of the peak sound pressure Δp_m. A: Case A with fine resolution. A′: Case A with coarse resolution; C: Case C with fine resolution; C′: Case C with coarse resolution.

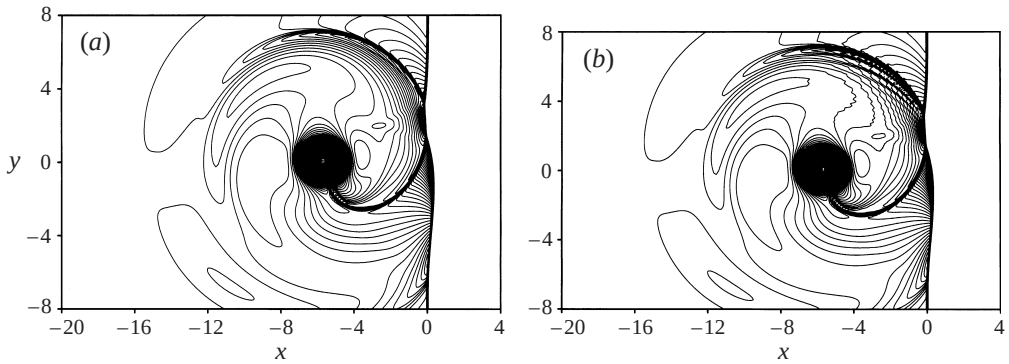

FIGURE 10. Accuracy tests. Density fields. Case A, $t = 8.0$: (*a*) fine resolution, (*b*) coarse resolution. The contour levels are from $\rho_{\min} = 0.92$ to $\rho_{\max} = 1.55$ with an increment of 0.0053.

described before (Cases A, B and C). That is, through the shock–vortex interaction, a Mach reflection occurs and two sliplines emanate from triple points which are clearly seen in the isopycnics of figure 11(*a*). The sound pressure field in figure 11(*b*) is similar to that of the inviscid Euler simulation of Ellzey *et al.*

Schlieren pictures obtained from the calculated density fields at $t = 7.0$ and $t = 10.3$ are presented in figure 12. Again we can see the two reflected shock waves and the two sliplines emanating from the triple points. The precursor appears ahead of the reflected shock waves and propagates radially outward from the vortex centre with increasing time. If we compare our computational schlieren pictures in figure 12 with the experi-

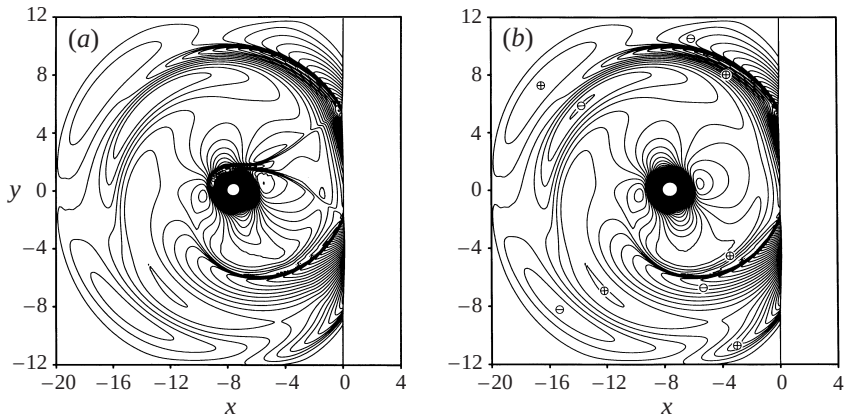

FIGURE 11. Density and sound pressure fields at the same conditions as the experiment of Dosanjh & Weeks (1965). $M_s = 1.29, M_v = 0.39, Re = 800$. $t = 10.3$. (*a*) Isopycnics. The contour levels are from $\rho_{\min} = 1.26$ to $\rho_{\max} = 1.60$ with an increment of 0.0029. (*b*) Isobars of Δp. The contour levels are from $\Delta p_{\min} = -0.16$ to $\Delta p_{\max} = 0.24$ with an increment of 0.0033.

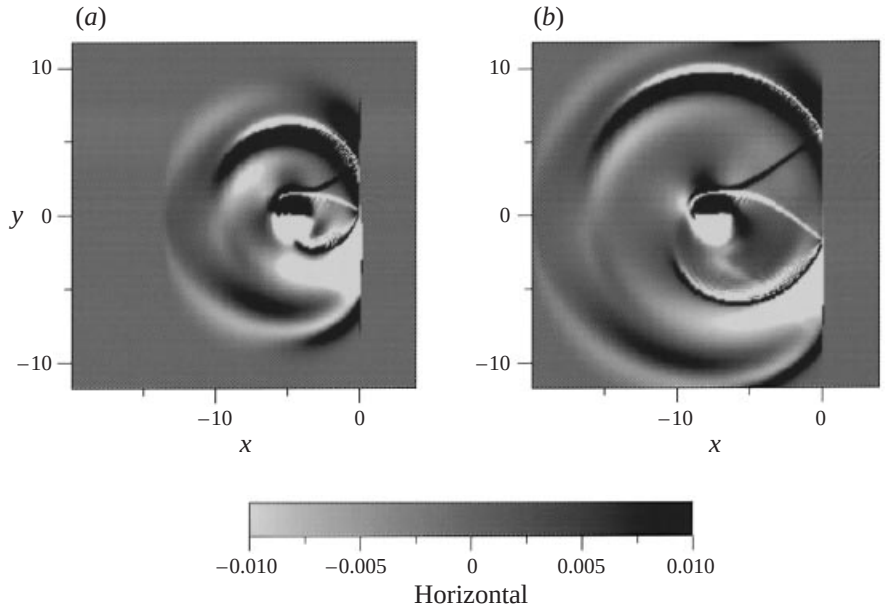

FIGURE 12. Computational schlieren pictures obtained from $\partial\rho/\partial y$.
$M_s = 1.29, M_v = 0.39, Re = 800$. (*a*) $t = 7.0$, (*b*) $t = 10.3$.

mental schlieren picture shown in figure 2(*b*) of Dosanjh & Weeks (1965), we observe a few differences, apart from the fact that the initial vortex in the experiment appears as a spiral, while in the simulation it is circular. First, in the simulation two reflected shock waves and two sliplines emanating from the triple points are clearly observed, but in the experiment they are not apparent. This difference may not be due to the Reynolds number effect, because both the present Navier–Stokes result and the inviscid Euler result of Ellzey *et al.* give the Mach reflection. (Ellzey *et al.* did not present the density field and thus the sliplines emanating from the triple points were not shown.) Second, in the experiment only one acoustic wave is visible which expands radially

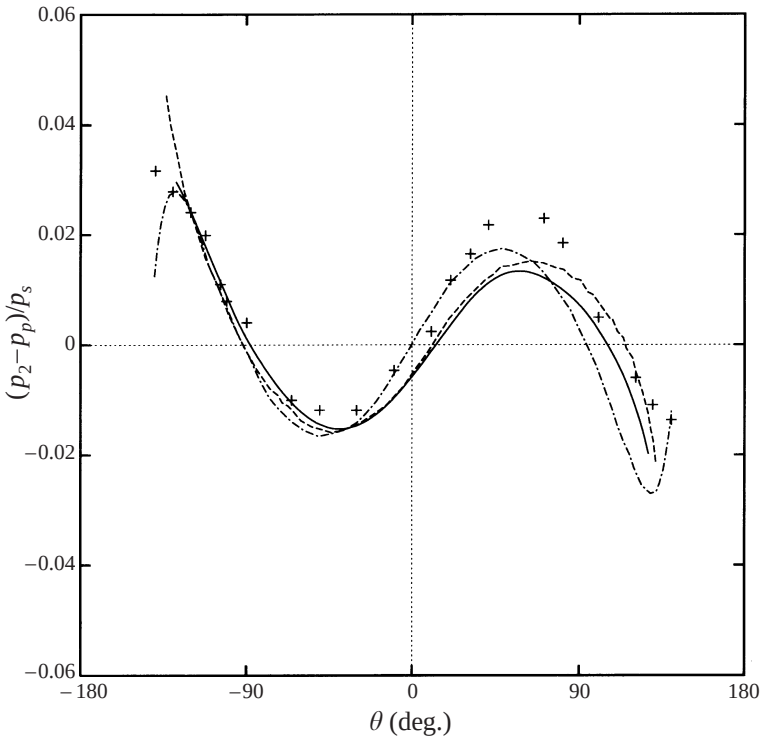

FIGURE 13. Comparison of the present Navier–Stokes result (————) with experiment (Dosanjh & Weeks 1965, +), theory (Ribner 1985, – · – · –) and the Euler result (Ellzey *et al.* 1995, — — — — —). The symbol p_p denotes the pressure of the precursor, p_2 the pressure of the second sound, and p_s the pressure behind the shock wave.

outward from the vortex centre, while in the simulation three waves are observed: the precursor and the two reflected shock waves 1 and 2. The sound pressure distributions obtained by the inviscid Euler simulation of Ellzey *et al.* also showed the three waves.

3.2.2. *Circumferential pressure distributions*

Presented in figure 13 is the comparison of the circumferential distributions of the pressure amplitude, $(p_2 - p_p)/p_s$, among the present Navier–Stokes result, the experimental result of Dosanjh & Weeks, the Euler result of Ellzey *et al.* and the theoretical result of Ribner. The symbols p_2 and p_p denotes the pressures of the second sound and the precursor, respectively. In the experiment, an interferogram was taken when the radius of the 'acoustic wave' was approximately ten times that of the vortex core. The density amplitude distribution around the circumference of the acoustic wave was determined from the interferogram and converted to pressure amplitude distribution by using the acoustic approximation, $\Delta p = a^2 \Delta\rho$, where a is the speed of sound. Ellzey *et al.* noticed that the density difference measured from the interferogram is the difference between the amplitude of the acoustic front and the amplitude of the precursor. They scanned the sound pressure field to determine the radii where the amplitudes of the precursor and the second sound are respectively maximum, and calculated the difference in the sound pressures at these radii. Their result (dashed line) together with the results of Dosanjh & Weeks (+) and Ribner (chain-dotted line) are replotted in figure 13 from figure 8 of Ellzey *et al.* (1995).

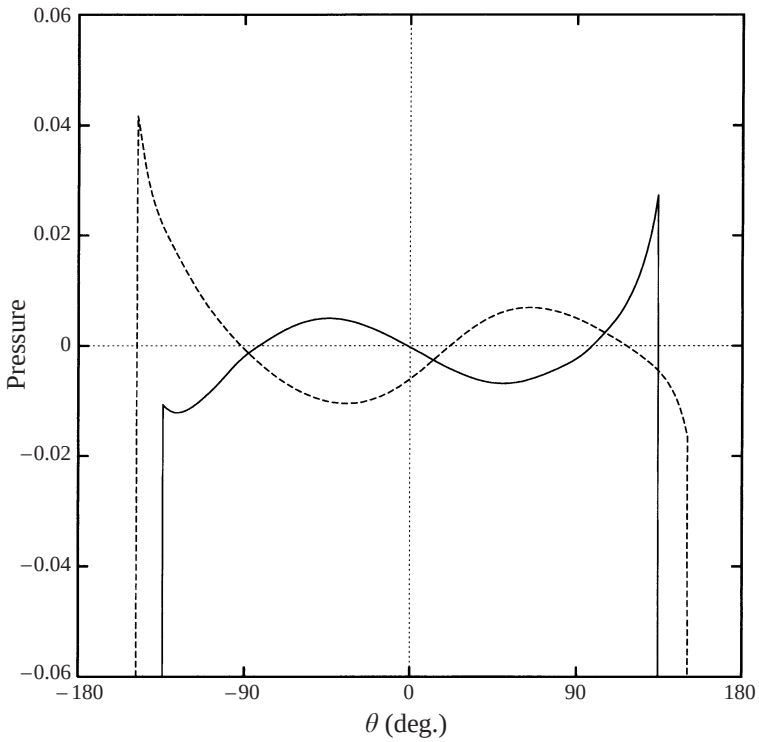

FIGURE 14. Circumferential distributions of the sound pressure Δp. $t = 10.3$. ———, precursor ($r = 10.8$); — — — — —, the second sound ($r = 8.8$).

As the flow fields in the schlieren pictures are different for the experiment of Dosanjh & Weeks and the present simulation, the same definition of the radius of the 'acoustic wave' as in the experiment was not possible in this study. Ellzey *et al.* identified the second sound as the acoustic wave to be compared with that of Dosanjh & Weeks. However, as seen in figure 12, it is difficult to determine definitively the radius of the second sound from the schlieren pictures. In this study, we define the radius of the 'acoustic wave' as the distance between the vortex centre and the upper reflected shock wave measured at $\theta = -90°$. As seen from figures 11(*b*) and 12(*b*), the flow field where the radius of 'acoustic wave' is about ten times that of the vortex core is achieved in this simulation approximately at $t = 10.3$. The radii of the precursor and the second sound were determined in the same way as in Ellzey *et al.* For reference, the circumferential distributions of the sound pressure of the precursor (solid line) and the second sound (dashed line) are presented in figure 14. As seen from figure 13, the present Navier–Stokes result shows good agreement with the experiment. The quantitative difference between the simulation and the experiment may be considered not large if we take into consideration the differences of the flow field shown in the schlieren pictures. The quantitative difference between the present Navier–Stokes result and the Euler result is small, suggesting a small effect of the Reynolds number.

3.2.3. *Discussion*

At present we have no definite explanation for the differences in the schlieren pictures for the experiment and the simulation. As one possible reason, we assumed that the specified value of $M_v = 0.39$ might be too large. In the experiment, the airfoil

angle of attack was set to provide the maximum possible vortex tangential velocity, which yielded $M_v = 0.39$ when $M_s = 1.29$ (Weeks & Dosanjh 1967). As was seen in figure 8, with a decrease in M_v, the strengths of the reflected shock waves become smaller. Therefore, for a sufficiently small M_v the reflected shock waves may become very weak, and thus it may be difficult to detect them in a schlieren picture unless the sensitivity is very high. For such a small M_v the sliplines emanating from the triple points may also be very weak. In order to confirm this possibility, an additional simulation with the same shock Mach number $M_s = 1.29$ but with a much smaller vortex Mach number $M_v = 0.05$ was performed. The result showed, as expected, that for this small M_v the reflected shock waves and the sliplines were not detected in a schlieren picture without much higher sensitivity than that in figure 12. However, for this case the pressure amplitude $(p_2 - p_p)/p_s$ also became very small, resulting in the large deviation of the pressure amplitude from the experiment. Therefore, the assumption that the specified value of $M_v = 0.39$ might be too large was not validated. In order to solve the discrepancy in the schlieren pictures, further computational as well as experimental studies are required.

4. Results for the case of a pair of vortices

For the case of the interaction between a pair of vortices and a shock wave, two types of flow fields are considered, depending on whether the pair moves, by its self-induced velocity, in the same direction as the shock wave (hereafter referred to as a passing vortex pair) or in the opposite direction (a collision vortex pair). In this study, as noted in § 2, a coordinate system which moves with a shock wave is adopted and the position of the shock wave is fixed to be $x = 0$. The region of a negative x is assumed to be downstream of the shock wave. Therefore, the upper vortex is clockwise for a collision type while the lower vortex is clockwise for a passing type. For each type, six different combinations of M_s, M_v and Re (Case A to Case F listed in table 1) were examined, though the Reynolds number effect was found to be negligible as in the case of a single vortex. In computations, we used the same mesh system as in the case of a single vortex and did not assume the symmetry of the flow field with respect to the $y = 0$ plane. Nevertheless, as will be seen throughout (for example, figures 15, 20 and 23), the results show beautiful symmetry, supporting the numerical accuracy of this computation. In § 4.1, characteristic features of flow fields and sounds generated for the case of a passing vortex pair are discussed. Then, in § 4.2, computational results for the case of a collision vortex pair are presented. For both the generation and nature of the sounds are shown to be related not only to the deformation and reflection of the shock wave but also to the propagation of the reflected shock waves.

4.1. *Basic structure of sound generation for a passing vortex pair*

4.1.1. *Initial evolution of shock–vortex interaction*

A typical example of the time development of the sound pressure field for the case of a passing vortex pair is presented in figure 15 for Case C. The shock wave deformation caused by the interaction with the pair of vortices is schematically presented in figure 16, where time increases from (*a*) to (*e*). As seen from figures 15(*a*) and 16(*a*), immediately after the beginning of the interaction, a rarefaction region is produced near the $y = 0$ plane while two compression regions are produced at the upper and lower sides of the rarefaction region. Then, with the development of the interaction, new rarefaction regions appear outside each compression region (figure 15*b*). As a

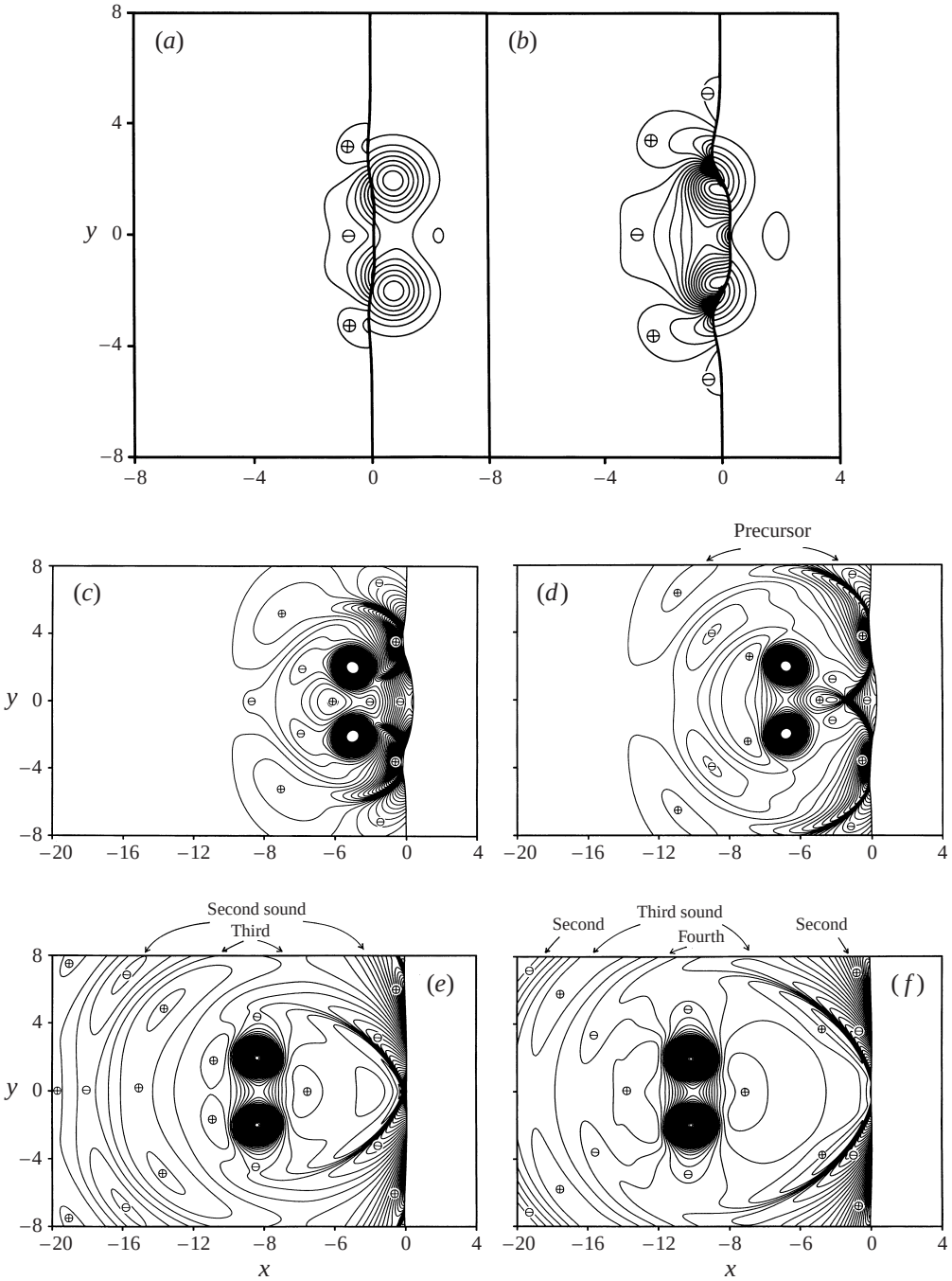

FIGURE 15. Time development of sound pressure fields for a passing vortex pair. Isobars of Δp. Case C. (*a*) $t = 1.0$, (*b*) $t = 2.0$, (*c*) $t = 5.0$, (*d*) $t = 7.0$, (*e*) $t = 11.0$, (*f*) $t = 13.0$. The contour levels are from $\Delta p_{\min} = -0.44$ to $\Delta p_{\max} = 0.12$ with an increment of 0.0112 for (*a*) and (*b*), from $\Delta p_{\min} = -0.14$ to $\Delta p_{\max} = 0.12$ with an increment of 0.0039 for (*c*) and (*d*), and $\Delta p_{\min} = -0.16$ to $\Delta p_{\max} = 0.08$ with an increment of 0.0029 for (*e*) and (*f*).

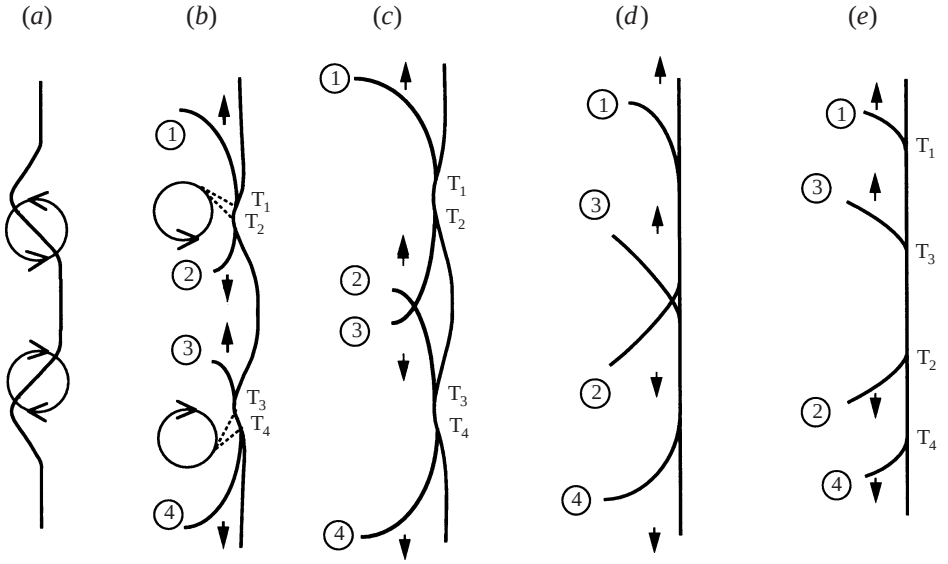

FIGURE 16. Temporal variation of shock wave deformation due to the interaction with a passing pair of vortices. Case C. T_1 to T_4 denote the triple points.

result, the circumferential variation of the sound pressure, when viewed from the mid-point between the two vortices, alternates from negative (rarefaction region just behind the upper part of the shock wave) to positive to negative (rarefaction region near the $y = 0$ plane) to positive to negative (rarefaction region just behind the lower part of the shock wave). This is the initial circumferential variation of the precursor. With further development of the interaction, the shock wave in the compression regions continues to deform, and eventually two sets of reflected shock waves are radiated: one in the upper ($y > 0$) region and the other in the lower ($y < 0$) region (figures 15*c* and 16*b*). Each set consists of two components, which are numbered 1 and 2 for the upper set and 3 and 4 for the lower set in figure 16. The essential mechanism of the generation of reflected shock waves 1 to 4 is the same as that in the case of a single vortex shown in figures 3 and 4, except that the sense of rotation of the lower vortex in this case is opposite to that of the single vortex.

4.1.2. *Propagation of reflected shock waves and evolution of sound waves*

With increased time, the reflected shock waves 1 and 3 move upward, while 2 and 4 move downward. As a result, the reflected shock waves 2 and 3 cross each other (figures 15*d*, *e* and 16*c*, *d*), and then pass through each other (figures 15*f* and 16*e*). As noted in the case of a single vortex, the propagation velocities of reflected shock waves 1 and 4 are larger than those of 2 and 3, respectively, and thus 2 and 3 do not catch up with 1 and 4.

The sound pressure field in figure 15 shows that the rarefaction region of the precursor which is located near the $y = 0$ plane at initial times (figure 15*a*, *b*) tends to die out with increasing time (figure 15*c*, *d*), and that eventually the sound pressure Δp near the $y = 0$ plane takes a small positive value. Figure 15(*d*) shows that the circumferential variation of the second sound is different from the precursor. Figure 15(*d*) also shows that new compression regions appear behind the rarefaction regions of the second sound, indicating that the third sound is just being generated. With a further increase in time, the third sound develops, and we can see from

figures 15(*e*) and 15(*f*) that the circumferential variation of Δp of the third sound has the same sign as the precursor. Figure 15(*f*) also shows that the fourth sound is generated and the circumferential variation of Δp of the fourth sound is opposite in sign to the precursor. It is worth noting in figure 15(*f*) that, very close to the pair of vortices, two compression regions exist upstream and downstream of the pair, while two rarefaction regions exist on the upper and lower sides of the pair. At first glance, this result suggests that a fifth sound having a quadrupolar nature is generated. However, this is not the case because these regions do not propagate radially from the pair of vortices but instead move along with it. Therefore, for the case of a passing vortex pair, sounds are produced four times (from the precursor to the fourth sound) through the interaction between the shock wave and the pair of vortices.

4.1.3. *Sound wave evolution relative to shock wave reflection*

The characteristic nature of sound generation for the passing vortex pair mentioned above is schematically presented in figure 17(*a*), where a solid circle on the $y = 0$ plane denotes a small negative value of Δp while an open circle denotes a small positive one. It should be noted from the figure that the rarefaction regions of the precursor and the compression regions of the second sound are respectively located ahead of and behind reflected shock wave 1 (and 4), and that the rarefaction regions of the third sound and the compression regions of the fourth sound are located respectively ahead of and behind reflected shock wave 3 (and 2). This result suggests that the generation and the nature of the sounds in this case may be closely related to the generation of the reflected shock waves. In other words, the generation of additional sounds may not be expected in this case because further generation of reflected shock wave may not be expected.

4.1.4. *Effects of M_s, M_v and Re*

Typical examples of the sound pressure fields for different combinations of M_s, M_v and Re are presented in figure 18: Case A in figure 18(*a*), Case D in figure 18(*b*) and Case F in figure 18(*c*). By comparing the flow fields in figure 18 with that in figure 15(*d*) for Case C, we can see that the essential features of the sound generation are not affected by the parameters. In figure 18(*b*) for Case D, Δp of the precursor is largest near the $y = 0$ plane, which looks different from the characteristic nature of the sound shown in figure 17(*a*). This is because rarefaction near the $y = 0$ plane produced at an initial time of the interaction is very weak because of the weak shock wave ($M_s = 1.05$) and, soon after the generation, the rarefaction region is replaced by the compression region produced by the translational motion of the pair of vortices. In figure 18(*c*) for Case F, the shock Mach number is small as in Case D, but in this case M_v is also small; compression produced by the translational motion of the pair of vortices is not as large as in Case D. It should be noticed that in all cases the sign of Δp near the $y = 0$ plane is not affected by the parameters.

4.1.5. *Density fields visualized by shadowgraphs*

Presented in figure 19 are shadowgraphs for different combinations of M_s and M_v but for fixed values of $Re = 400$ and $t = 9.0$ we can see that for the passing vortex pair, the reflected shock waves and the sliplines are clearly captured in shadowgraphs, but that the existence of and the distinction between the precursor and the second sound are not very clear. This is in contrast with the collision type shown later (figure 28). By comparing figure 19 with figure 8 for a single vortex, we can also see that the patterns of the reflected shock waves and the sliplines generated for the

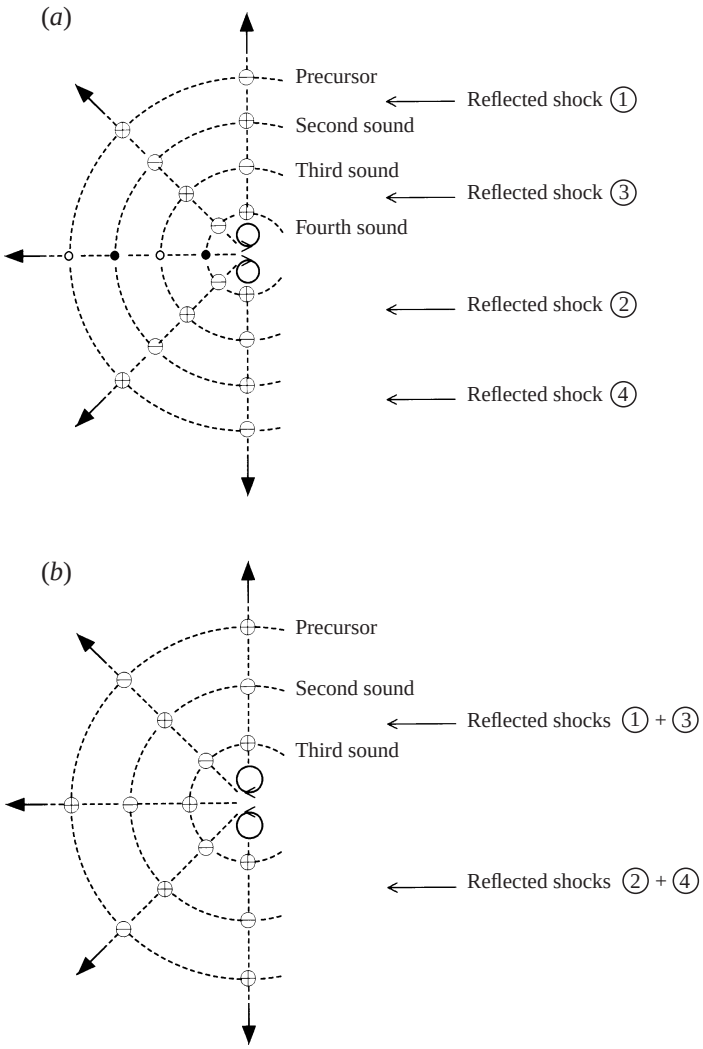

FIGURE 17. Basic nature of sound generation for the case of a pair of vortices interacting with a shock wave. Case C: (*a*) passing type, (*b*) collision type; ⊕ compression region: ⊖, rarefaction region.

passing type are basically determined by the superposition of those produced by each single vortex of a pair. The strong compression region of the precursor behind the incident shock wave, which is observed in the negative y-plane in figure 8 for the case of a single vortex, is not produced for the passing type. In agreement with the flow feature shown in figure 16, four triple points and thus four sliplines are observed for $M_s = 1.2$ (figure 19 *a*, *b*).

4.2. *Basic structure of sound generation for a collision vortex pair*

In contrast with the passing vortex pair mentioned above, flow structures produced by the interaction for a collision vortex pair, especially shock wave deformation, are affected by the Mach numbers, and can be categorized into the following three types depending on the combinations of M_s and M_v.

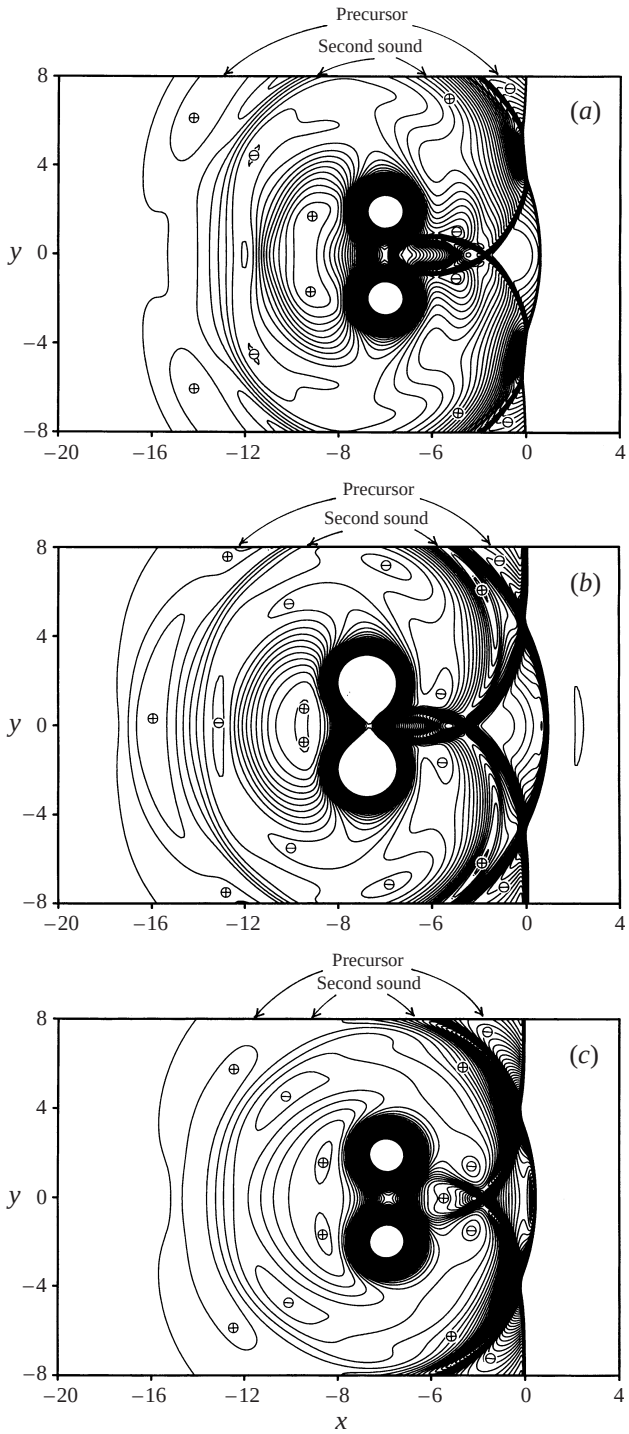

FIGURE 18. Sound pressure fields for a passing vortex pair. Δp. (*a*) Case A. The contour levels are from $\Delta p_{\min} = -0.25$ to $\Delta p_{\max} = 0.12$ with an increment of 0.0044. (*b*) Case D. The contour levels are from $\Delta p_{\min} = -0.075$ to $\Delta p_{\max} = 0.06$ with an increment of 0.0018. (*c*) Case F. The contour levels are from $\Delta p_{\min} = -0.055$ to $\Delta p_{\max} = 0.04$ with an increment of 0.000 09.

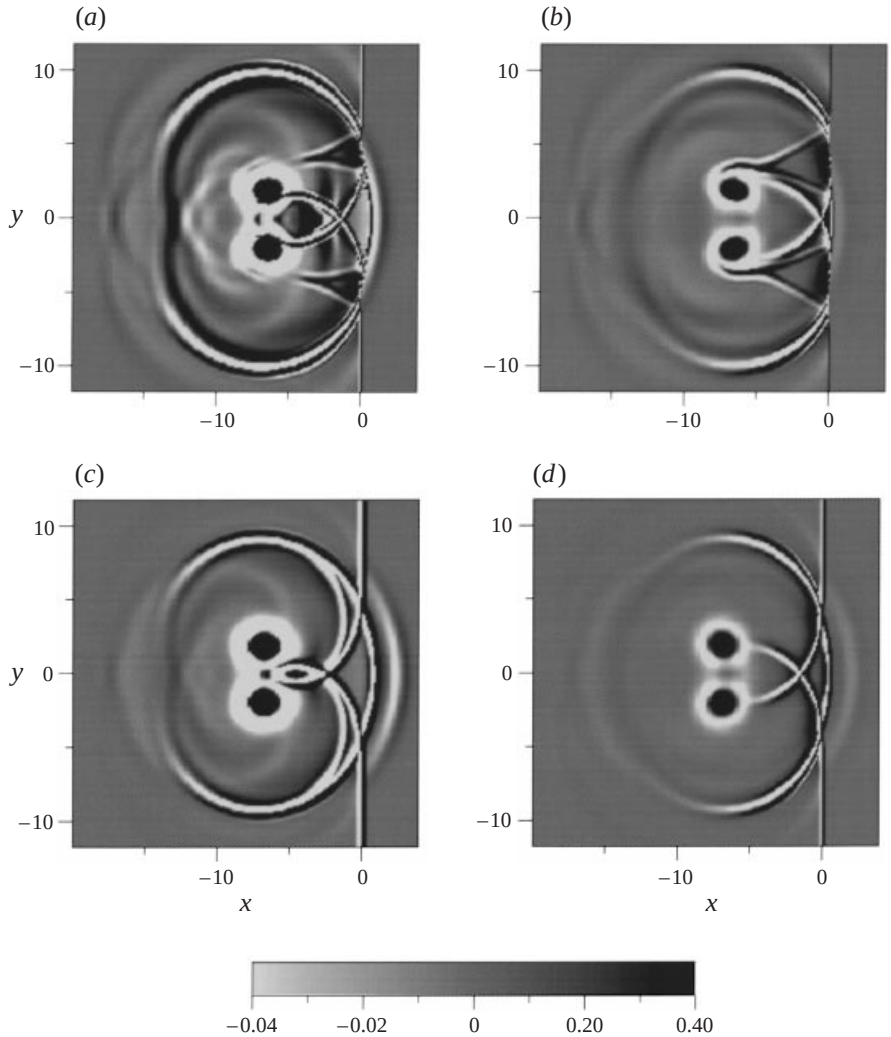

FIGURE 19. Shadowgraphs obtained from $\nabla^2\rho$ for the case of passing vortex pair. $Re = 400, t = 9.0$. (*a*) Case A, (*b*) Case B, (*c*) Case D, (*d*) Case E.

Type I: Mild interaction without shock wave focusing. Cases B and C ($M_s = 1.2$ and $M_v = \pm 0.25$).

Type II: Intermediate interaction with shock wave focusing. Cases E and F ($M_s = 1.05$ and $M_v = \pm 0.25$).

Type III: Strong interaction with shock wave focusing and additional expansion waves. Case A ($M_s = 1.2$ and $M_v = \pm 0.5$) and Case D ($M_s = 1.05$ and $M_v = \pm 0.5$).

4.2.1. *Type I: mild interaction* (*Cases B and C*)

Evolution of shock-vortex interaction and propagation of reflected shock waves. A typical example of the time development of the sound pressure field for the case of a collision vortex pair is presented in figure 20 for Case C. The time development of shock wave deformation caused by the interaction is schematically presented in figure 21. As seen from figures 20(*a*) and 21(*a*), immediately after the beginning of the interaction, a compression region is produced near the $y = 0$ plane while two

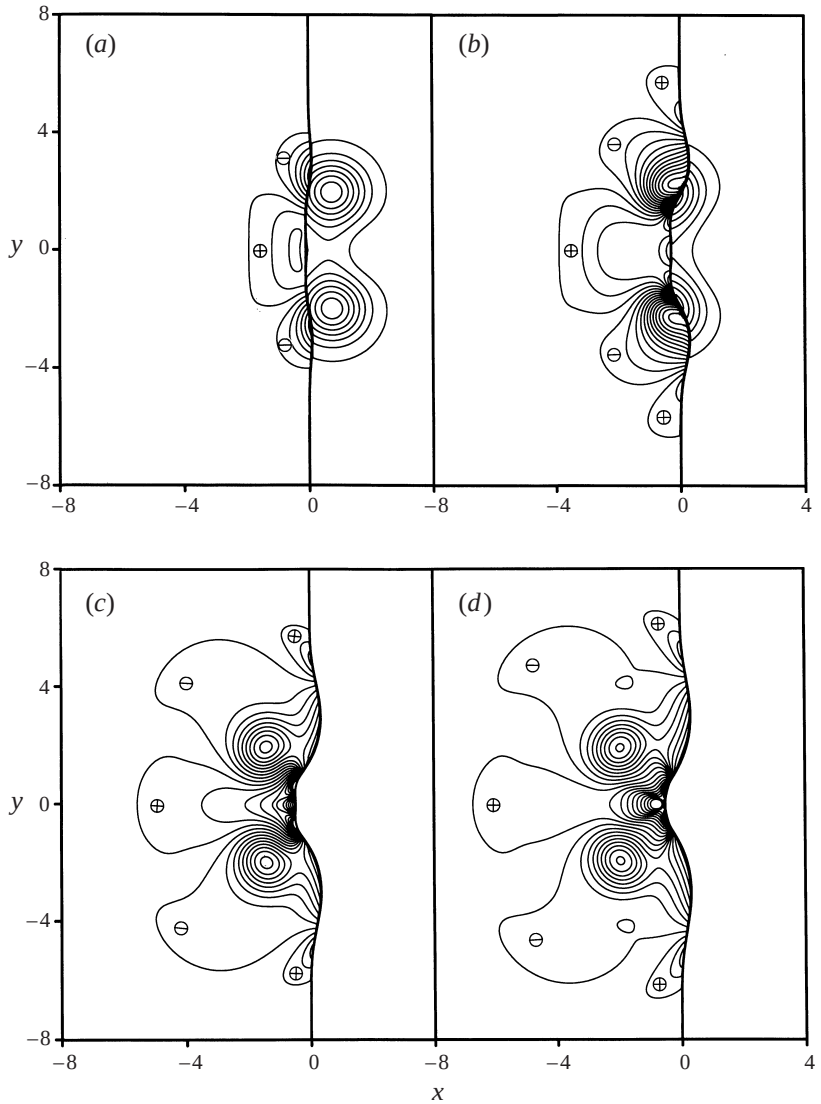

FIGURE 20 (*a–d*). For caption see facing page.

rarefaction regions are produced at the upper and the lower sides of the compression region. Then, with the development of the interaction, new compression regions appear outside each rarefaction region (figure 20*b*). As a result, the circumferential variation of the sound pressure becomes alternating. This alternating variation of Δp of the precursor along the circumferential direction is in contrast with that in the passing vortex pair discussed in the previous section (figure 15*b*). In addition, unlike the passing case, the compression region of the precursor near the $y = 0$ plane does not tend to die out with increasing time, as is seen in figure 20(*c*) to 20(*h*). With further development of the interaction, the shock wave in the compression region near the $y = 0$ plane deforms more and more, and eventually two sets of reflected shock waves are radiated, as seen in figures 20(*c*) and 21(*b*). Because the senses of rotation of the two vortices are opposite to those in the passing case, reflected shock

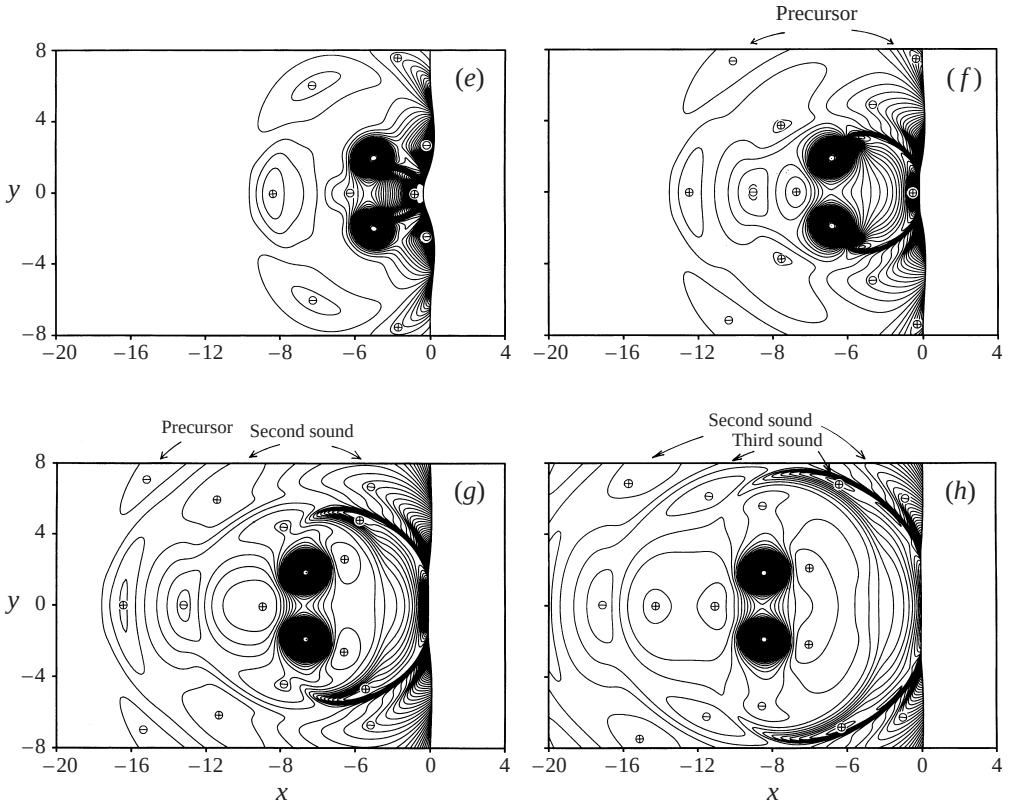

FIGURE 20. Time development of sound pressure fields for a collision vortex pair (Type I. mild interaction). Δp. Case C. (*a*) $t = 1.0$, (*b*) $t = 2.0$, (*c*) $t = 3.2$, (*d*) $t = 3.8$. (*e*) $t = 5.0$, (*f*) $t = 7.0$, (*g*) $t = 9.0$, (*h*) $t = 11.0$. The contour levels are from $\Delta p_{\min} = -0.44$ to $\Delta p_{\max} = 0.14$ with an increment of 0.02 for (*a*) and (*b*), from $\Delta p_{\min} = -0.44$ to $\Delta p_{\max} = 0.16$ with an increment of 0.0167 for (*c*) and (*d*), from $\Delta p_{\min} = -0.16$ to $\Delta p_{\max} = 0.12$ with an increment of 0.0044 for (*e*) and (*f*), from $\Delta p_{\min} = -0.16$ to $\Delta p_{\max} = 0.10$ with an increment of 0.0033 for (*g*) and (*h*).

waves 3 and 4 in this case correspond, respectively, to 1 and 2 in the case of a single vortex shown in figure 4. As in the passing case, reflected shock waves 2 and 3 cross (figures 20(*d*) and 21(*c*)) and then pass through each other (figures 20(*e*) and 21(*d*)). In contrast with the passing case, the propagation velocity of shock wave 3 is larger than that of shock wave 1, and thus shock wave 3 approaches shock wave 1 with further increasing time (figures 20*f–h* and 21*e*), and eventually the two shock waves 1 and 3 merge into a single, upward moving shock wave. Similarly, shock waves 2 and 4 merge into a single, downward moving shock wave. Figure 20(*f*) shows that the second sound is generated after the precursor and the circumferential variation of the second sound is in contrast with the precursor. Figures 20(*f*) and 20(*g*) show that the third sound develops and that the circumferential variation of Δp of the third sound is of the same sign as the precursor. In figure 20(*h*), as in the passing case, we can see two compression and two rarefaction regions which move with the pair of vortices. Again, the compression regions exist upstream and downstream of the pair, respectively, with two rarefaction regions on the upper and lower sides of the pair. Therefore, for Type I, acoustic sounds are observed three times through the shock–pair of vortices interaction.

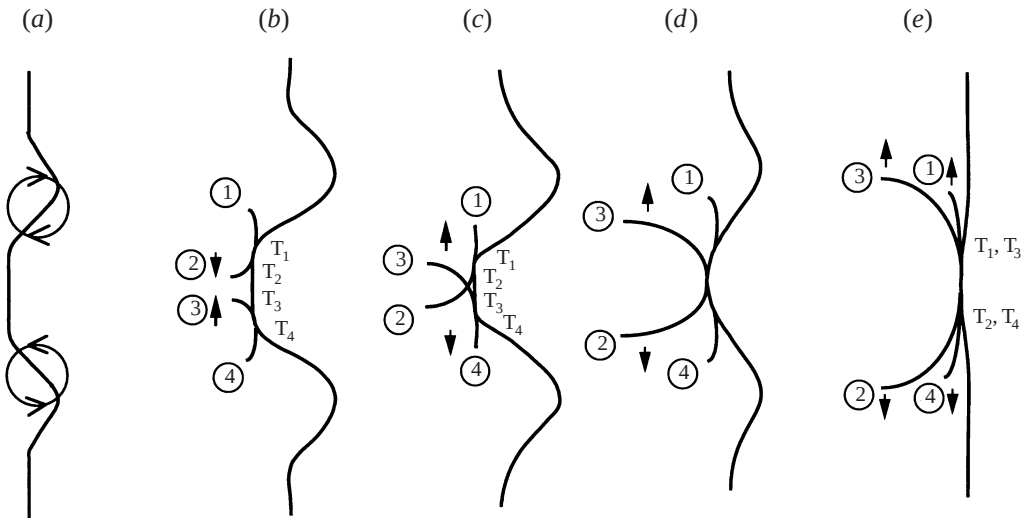

FIGURE 21. Temporal variation of shock wave deformation due to the interaction with a pair of vortices. Collision type. Type I (mild interaction).

Sound wave evolution relative to shock wave reflection. The characteristic nature of sound generation for the collision vortex pair for Case C is given in figure 17(*b*) which shows that the rarefaction regions of the second sound and the compression regions of the third sound are located respectively ahead of and behind the merged reflected shock waves $1+3$ in the $y>0$ region and $2+4$ in the $y<0$ region; the generation and the nature of the acoustic waves for the collision and the passing types may be closely related to the generation of the reflected shock waves. The generation of additional sounds may not be expected for Type I because further generation of reflected shock waves as well as other sources of sounds may not be expected, in contrast to Type III discussed later.

It should be noted that the relation between the sounds and the reflected shock waves shown in figure 17(*b*) is the same as that shown in the lower half of figure 6(*a*) for the case of a single vortex, if the merged shock wave 1+3 (or 2+4) in figure 17(*b*) is replaced with reflected shock wave 2 in figure 6(*a*). This result strongly suggests the possibility that the acoustic wave may be generated three times for the case of a single vortex, as already noted in § 3.1.3.

4.2.2. *Type II: intermediate interaction* (*Cases E and F*)

A typical example of the time development of the flow field for the case of the intermediate interaction is presented in figures 22 and 23 for Case F. In figure 22, the flow fields at an early stage of the flow development are shown, and the figures on the left-hand side are isopycnics while those on the right-hand side are isobars of the sound pressure Δp. The variation of the sound pressure is generally much smaller than that of the overall pressure field near the vortices and near the shock waves. This is especially true at an early stage of the flow development in Cases E and F because both M_s and M_v are small. Therefore, in order to see the small variation of the sound pressure, the contour levels of Δp should be prescribed to be within a certain limit so that both larger and smaller values of the sound pressure than the prescribed range are not plotted. However, from the resulting figures obtained by imposing this limitation on the contour levels of Δp, it may be a little difficult

for readers to understand the overall flow structures; mild limits are imposed on the contour levels of the density field so that the overall flow structures can be seen from the isopycnics. The flow fields at a later stage are shown in terms of isobars only in figure 23. The time development of shock wave deformation caused by the interaction for Case F is also presented schematically in figure 24.

At a very early stage of the interaction, the shock wave deformation and the generation of the sound pressure (the precursor) are quite similar to those in Type I. With development of the interaction, the shock wave in the compression region near the $y = 0$ plane deforms, and two sets of reflected shock waves are released, as seen in figures 22(*b*) and 24(*b*). In this case, owing to the stronger effect of the pair of vortices than the shock wave, the shock wave diffracts more drastically than Type I and the distance between the triple points T_1 and T_2 becomes shorter; the two triple points move downward as if they were a single point (figure 24*c*). Similarly, T_3 and T_4 move upward as if they were a single point. With increasing time, the distance between the triple points T_1 (or T_2) and T_3 (or T_4) becomes shorter and shorter (figure 22*c*), and eventually vanishes (figures 22*d* and 24*d*). At that moment, the incident shock wave and the four reflected shock waves meet at a point; that is, shock wave focusing occurs. A similar phenomenon has been observed experimentally by Minota (1993) and computationally by Takayama *et al.* (1993), both in shock wave–vortex ring interactions. With further increasing time, shock wave 3 approaches shock wave 1 (figures 23 and 24*e*), and eventually the two merge. Similarly, shock waves 2 and 4 merge. As seen from figure 23, the sounds are generated three times through the shock wave–vortex pair interaction and, except for the appearance of shock wave focusing, the qualitative features of the sounds generated are the same for Type I and Type II.

4.2.3. *Type III: strong interaction* (*Cases A and D*)

A typical example of the time development of the flow field at early times of the strong interaction is presented in figure 25 for Case A. A schematic diagram of the time development of shock wave deformation for this case is presented in figure 26. As seen from figures 25(*a*) to 25(*d*), the flow fields at an early stage of the flow development are quite similar to those in the previous case of Type II: the schematic diagrams of shock wave deformation corresponding to figures 25(*a*) to 25(*d*) are the same as figures 24(*a*) to 24(*d*) and thus omitted in figure 26. Figure 25(*e*) shows that a focal region, denoted by FR in figure 26(*a*), is formed in this Type III case after the shock waves focus. With further increasing time, the reflected shock waves 1 and 3, and 2 and 4, respectively, merge into combined structures (figures 25*f* and 26*b*). The flow field with the focal region presented in figures 25(*f*) and 26(*b*) is quite similar to that produced by the focusing of a weak shock wave as observed by Sturtevant & Kulkarny (1976) in a shock tube experiment with a reflector, though the focusing mechanism is quite different. The shock structure in figure 25(*f*) and 26(*b*) is also quite similar to that observed by Inoue, Sakai & Nishida (1996, 1997) in their computation of shock wave focusing induced by a projectile in a parabolic or an accelerated motion. With a further increase in time, the reflected shock waves approach the incident shock wave, and the focal region disappears.

Figure 27 shows sound pressure fields at later times for Case A. As the contour levels of figure 27 are different from those of figure 25, the sound pressure field at $t = 6.0$ in figure 25(*f*) is replotted in figure 27(*a*) for reference. As seen from figure 27(*b*) and 26(*c*), in strong contrast with Type I and Type II, new rarefaction (expansion) waves are generated in a region surrounded by the pair of vortices and the reflected shock waves. In figure 26(*c*), the signs of Δp are also plotted. RW denotes

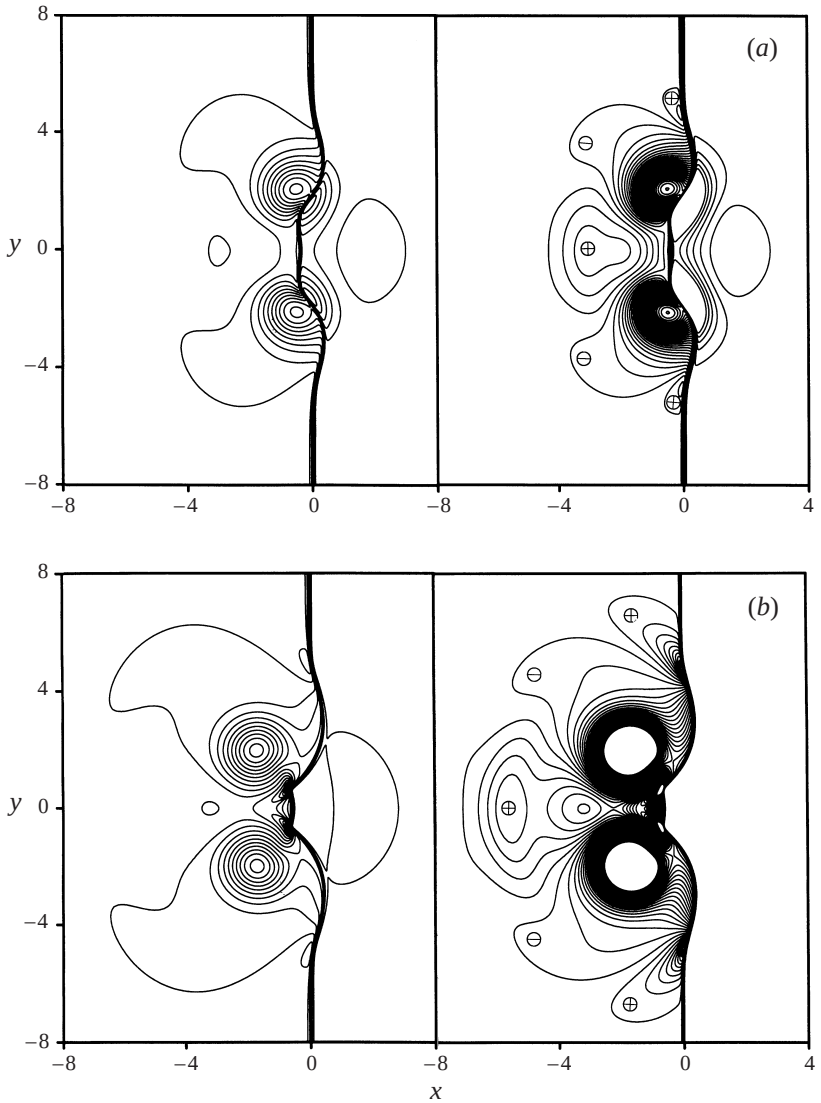

FIGURE 22 (*a*,*b*). For caption see facing page.

the rarefaction wave. The circles with arrows indicate the vortices. The rarefaction waves propagate away from the vortices towards the reflected shock waves, and as a result an additional rarefaction region is produced downstream of the pair of vortices (figure 26*d* and 27*c*, *d*). At the same time, as seen from figure 27(*c*) and 27(*d*), the sound pressure Δp along the $y = 0$ plane ahead of the pair shows the generation of a new rarefaction region ($-16 < x < -12$ in figure 27 *d*) after the third sound whose sign of Δp on the $y = 0$ plane is positive. As noted in the previous sections, Δp takes a positive value eventually both upstream and downstream of the pair of vortices. Therefore, the generation of new rarefaction regions both upstream and downstream of the pair of vortices suggests the possibility of the generation of the fourth sound. Figure 27(*d*) suggests that the circumferential variation of Δp of the fourth sound may be the same as that of the second sound. Unfortunately, simulation of the further

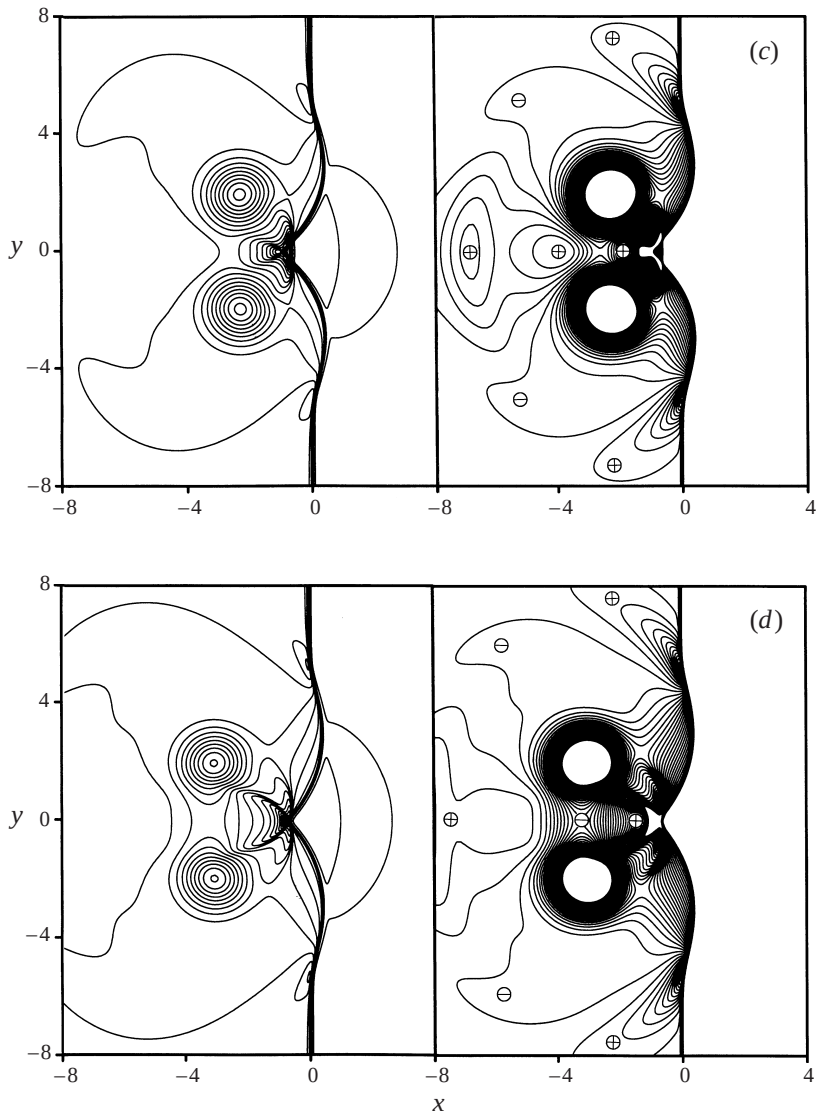

FIGURE 22. Time development of flow fields for a collision vortex pair (Type II intermediate interaction). Case F. Isopycnics (left column) and isobars (right column). (*a*) $t = 2.4$, (*b*) $t = 3.6$, (*c*) $t = 4.2$, (*d*) $t = 5.0$. The contour levels of isopycnics are from $\Delta\rho_{\min} = 0.92$ to $\Delta\rho_{\max} = 1.42$ with an increment of 0.01. The contour levels of isobars are from $\Delta p_{\min} = -0.10$ to $\Delta p_{\max} = 0.08$ with an increment of 0.0034 for (*a*) and from $\Delta p_{\min} = -0.05$ to $\Delta p_{\max} = 0.045$ with an increment of 0.0019 for (*b*) to (*d*).

development of the flow field requires a much wider computational domain, and thus was not possible with the performance of our supercomputer system; further confirmation of the generation of the fourth sound is left for future work. The flow features for Case D are quite similar to those for Case A.

4.2.4. *Density fields visualized by shadowgraphs*

Presented in figure 28 are shadowgraphs for different combinations of M_s and M_v but for fixed values of $Re = 400$ and $t = 9.0$. We can see that for the collision vortex

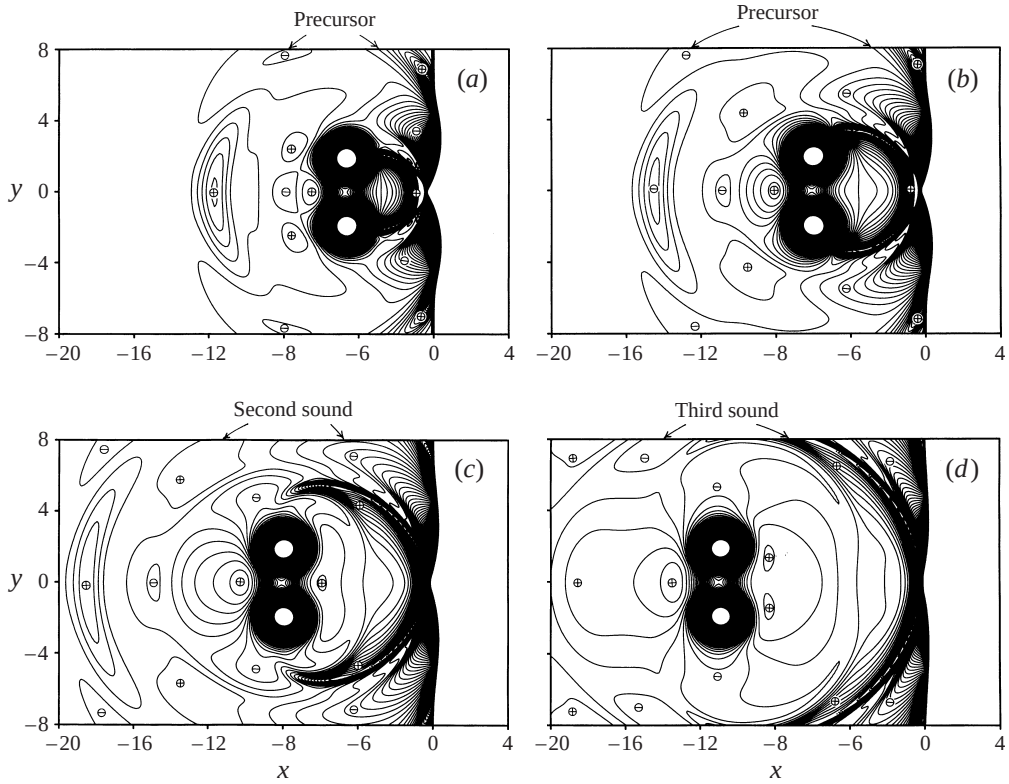

FIGURE 23. Time development of sound pressure fields, Δp, at a later stage for Case F. Collision type. Type II. (*a*) $t = 6.6$, (*b*) $t = 8.0$, (*c*) $t = 10.0$ (*d*) $t = 13.0$. The contour levels are from $\Delta p_{\min} = -0.07$ to $\Delta p_{\max} = 0.04$ with an increment of 0.001.

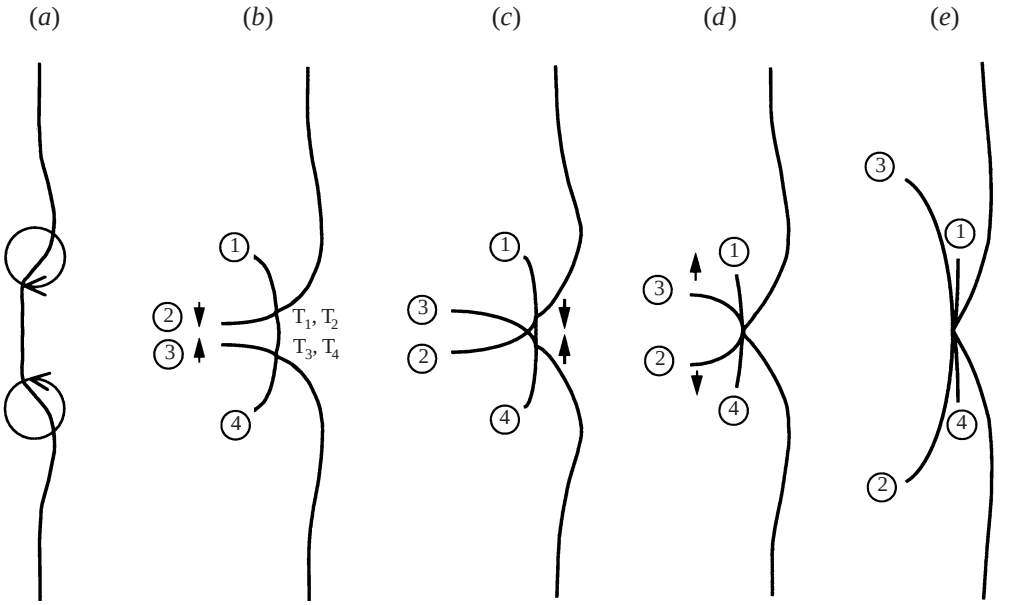

FIGURE 24. Temporal variation of shock wave deformation. Collision type. Type II (intermediate interaction).

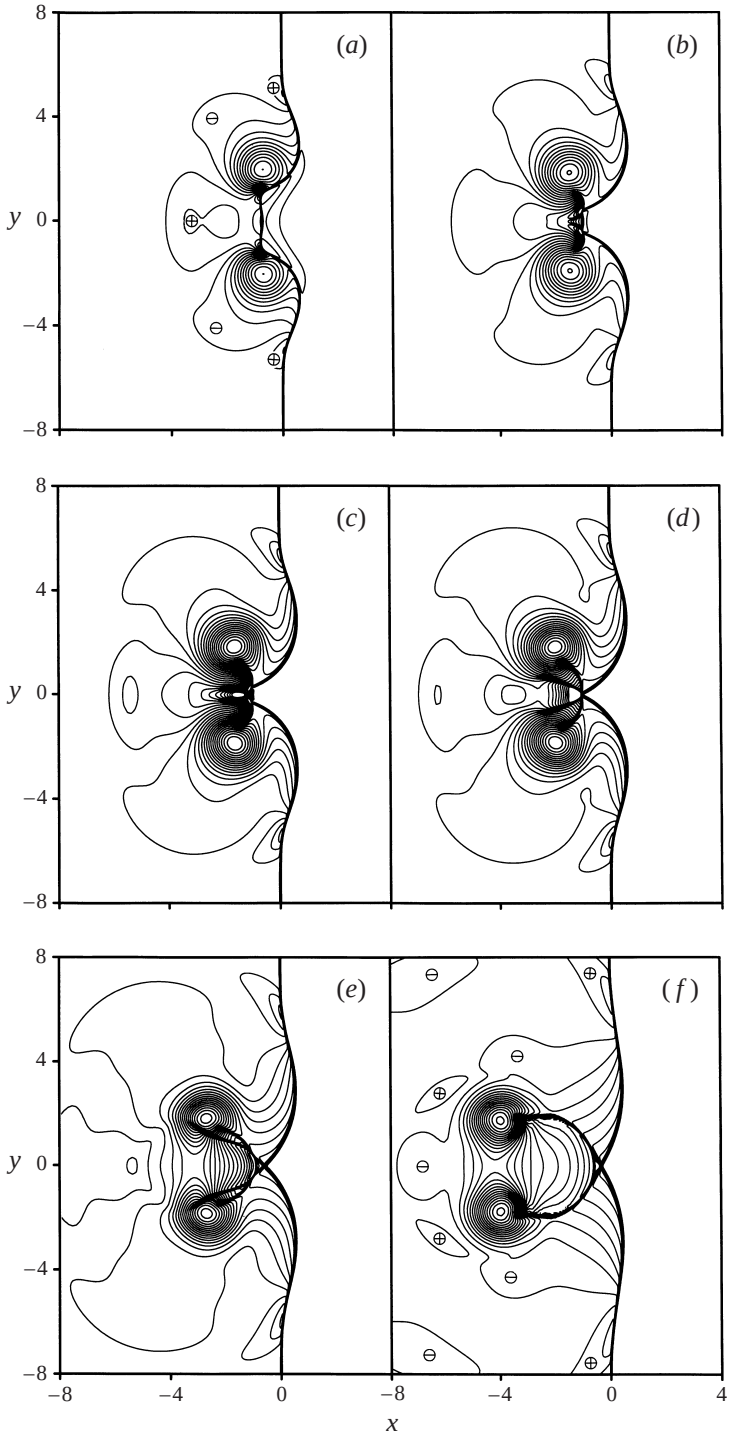

FIGURE 25. Time development of sound pressure fields, Δp, for Case A. Collision type. Type III. (*a*) $t = 2.4$, (*b*) $t = 3.2$, (*c*) $t = 3.4$ (*d*) $t = 3.8$, (*e*) $t = 4.6$, (*f*) $t = 6.0$. The contour levels are from $\Delta p_{\min} = -0.46$ to $\Delta p_{\max} = 0.30$, with an increment of 0.004 for (*a*) and (*b*) and 0.0028 for (*c*) to (*f*).

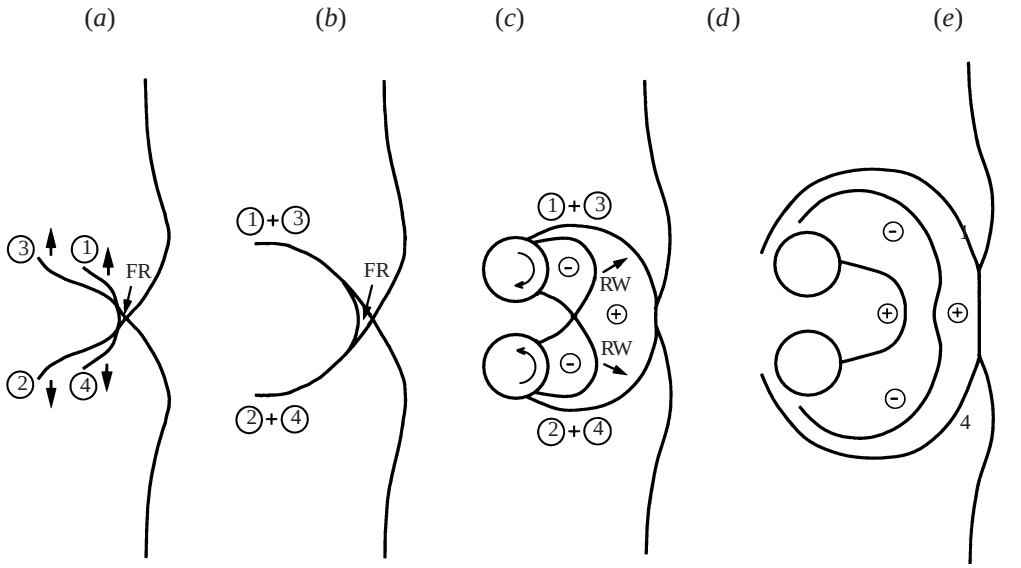

FIGURE 26. Temporal variation of shock wave deformation after focusing. Collision type. Type III (strong interaction). Parts (*a*) and (*b*) correspond to figure 25 (*e*) and 25 (*f*), respectively and (*c*) and (*d*) correspond to figure 27(*b*) and 27 (*c*, *d*), respectively. RW: rarefaction wave.

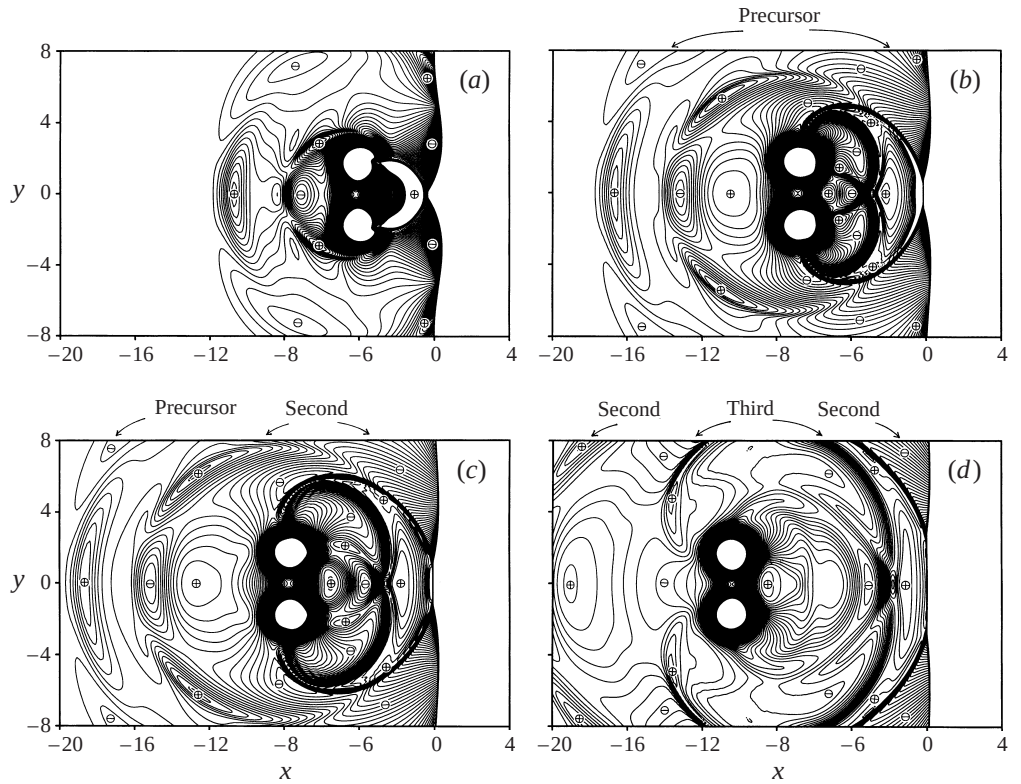

FIGURE 27. Time development of sound pressure fields at later times. Δp. Case A. Collision type. Type III. (*a*) $t = 6.0$, (*b*) $t = 9.0$, (*c*) $t = 10.0$, (*d*) $t = 13.0$. The contour levels are from $\Delta p_{\min} = -0.20$ to $\Delta p_{\max} = 0.07$ with an increment of 0.0034.

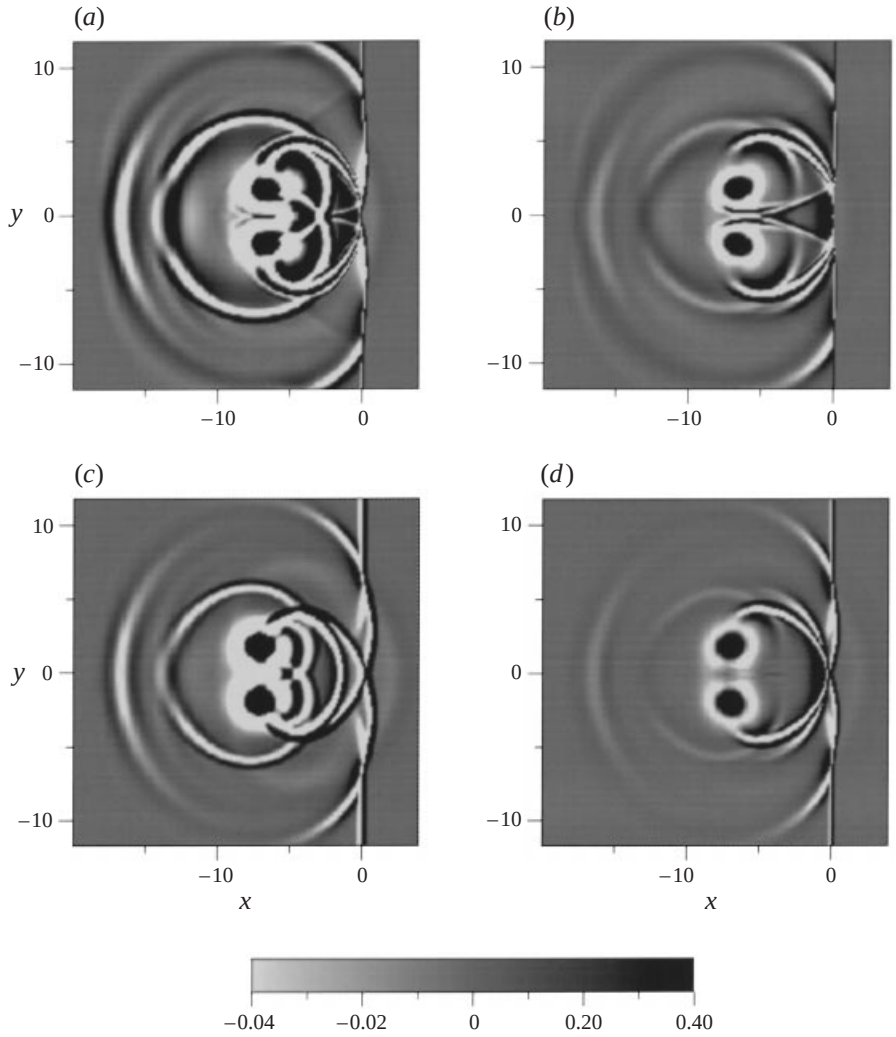

FIGURE 28. Shadowgraphs obtained from $\nabla^2\rho$ for the case of collision vortex pair. $Re = 400, t = 9.0$. (*a*) Case A, (*b*) Case B, (*c*) Case D, (*d*) Case E.

pair not only the reflected shock waves and the sliplines but also the precursor and the second sound are clearly captured in shadowgraphs, in contrast to the passing type shown in figure 19. By carefully comparing figure 28 with figure 8 for a single vortex, we can see that the nature of the flow fields at an early stage of flow development for the collision type are basically determined, as in the passing type, by the superposition of those produced by each single vortex of a pair, and that the generation of the precursor and the second sound for the collision type is fundamentally related to the generation of the precursor and reflected shock wave 1 for the single vortex shown in figure 4. In agreement with the flow features shown in figures 21 and 24, two triple points and thus two sliplines are observed for $M_s = 1.2$ (figure 28 *a*, *b*). This is in contrast with the passing type shown in figure 19(*a*, *b*) where four triple points and four sliplines are observed. It may be worth noting that additional waves, which are found to be rarefaction waves in Type III (figure 26), are also observed for Type

I (figure 28*b*) and Type II (figure 28*d*). The waves are not strong enough to form rarefaction waves for Type I and Type II because of the small value of M_v.

5. Concluding remarks

By using the direct Navier–Stokes simulation, two-dimensional flow fields produced by the interactions between a shock wave and a single vortex or a pair of vortices were studied. The effects of the strengths of shock waves and vortices on the flow fields are examined, and the basic nature of the near-field sound generated by the interactions was clarified in some detail. The results showed that larger M_v as well as M_s produce stronger compressions and rarefactions and thus larger magnitudes of the sound pressure. The effect of the Reynolds number based on the vortex core radius was found to be negligible, so far as the values of Re examined in this study are concerned.

For the case of a single vortex, acoustic waves were observed twice: the precursor and the second sound. Both sounds have a quadrupolar nature, but the circumferential variation of the sound pressure is opposite in sign. These results are in qualitative agreement with experimental observations (Hollingsworth & Richards 1955; Dosanjh & Weeks 1965) as well as the computational results by the Euler simulation of Ellzey *et al.* (1995). On the other hand, comparison of the present Navier–Stokes results with the experiment of Dosanjh & Weeks (1965) revealed a few differences. For example, in the computational schlieren pictures the precursor and two reflected shock waves (and two sliplines emanating from the triple points) are clearly observed, but in the experimental schlieren pictures only one acoustic wave is visible which expands radially outward from the vortex centre. This difference may not be due to the Reynolds number effect, because both the present Navier–Stokes simulation and the Euler simulation of Ellzey *et al.* give similar results. Somewhat surprisingly, the circumferential distributions of the pressure amplitude show good agreement between the experiment and the simulation. At present, the discrepancy between the simulation and the experiment remains unsolved; further computational and experimental studies are necessary. The comparison of the present Navier–Stokes results with the Euler results gives good agreement, suggesting the small effect of the Reynolds number in this problem. The comparison of the flow fields of a single vortex and a vortex pair of the collision type suggests that the third sound may be generated at later times for the case of a single vortex. However, confirmation of the third sound requires a much wider computational domain and thus is left for future work.

For the case of a vortex pair, the flow field produced by the interaction, and thus the sounds generated, show different characteristic features, depending on whether the pair moves in the same direction as the shock wave (passing type) or opposite to it (collision type). For the case of a passing vortex pair, sounds are found to be generated four times (from the precursor to the fourth sound). The essential features of the flow field for the passing case were not affected by M_s and M_v.

For the case of a collision vortex pair, the flow field produced by the interaction is found to be affected by M_s and M_v, and can be categorized into three types, so far as the parameters used in this study are concerned. In mild interaction (Type I), shock wave focusing does not occur, and the sounds are generated three times. In intermediate interaction (Type II), shock wave focusing occurs but acoustic sounds are generated three times as in Type I. The characteristic nature of the sounds in Type II is also the same as in Type I. In strong interaction (Type III), shock wave focusing occurs as in Type II. However, in contrast with Type II, the computational results for

Type III suggest the possibility of the generation of the fourth sound owing to the generation of additional rarefaction (expansion) waves.

The results for both a single vortex and a pair of vortices suggest that for shock wave–vortex interaction problems the generation and the nature of sounds may be closely related to the generation of (reflected) shock waves and expansion waves, though this may not be the only mechanism responsible for the generation of acoustic waves.

In this study, the basic nature of the near-field sounds was clarified in some detail both for a single vortex and for a pair of vortices. The study of the nature of the far field and the transition process from near to far fields requires a much wider computational domain and thus is left for future work. Also planned for future work is the confirmation of the third sound for a single vortex and the fourth sound for a vortex pair of collision type (Type III).

The authors express their sincere appreciation to Professor Katsuya Ishii, Faculty of Engineering, Nagoya University, for his kind advice and suggestions. Thanks are also given to Mr Sakari Onuma, Institute of Fluid Science, Tohoku University, for his technical assistance. The first author expresses his sincere gratitude to Asako Inoue for her continuous encouragement. Computations were performed with the CRAY C916 at the Institute of Fluid Science, Tohoku University.

REFERENCES

Bayliss, A. & Maestrello, L. 1981 Simulation of instabilities and sound radiation in a jet. *AIAA J.* **19**, 835–841.

Colonius, T., Lele, S. K. & Moin, P. 1994 The scattering of sound waves by a vortex: numerical simulations and analytical solutions. *J. Fluid Mech.* **260**, 270–298.

Dosanjh, D. S. & Weeks, T. M. 1965 Interaction of a starting vortex as well as a vortex street with a traveling shock wave. *AIAA J.* **3**, 216–223.

Ellzey, J. L., Henneke, M. R., Picone, J. M. & Oran, E. S. 1995 The interaction of a shock with a vortex: shock distortion and the production of acoustic waves. *Phys. Fluids* **7**, 172–184.

Filotas, L. T. 1967 Distortion of a shock wave traversed by a vortex. *UTIAS Tech. Note* 96.

Guichard, L., Vervisch, L. & Domingo, P. 1995 Two-dimensional weak shock-vortex interaction in a mixing zone. *AIAA J.* **33**, 1797–1802.

Hollingsworth, M. A. & Richards, E. J. 1955 A schlieren study of the interaction between a vortex and a shock wave in a shock tube. *Aeronaut. Res. Counc. Rep.* 17985, FM 2323.

Hollingsworth, M. A. & Richards, E. J. 1956 On the sound generated by the interaction of a vortex and a shock wave. *Aeronaut. Res. Counc. Rep.* 18257, FM 2371.

Inoue, O., Sakai, T. & Nishida, M. 1996 Shock wave focusing by a moving obstacle. *AIAA Paper* 96–2006.

Inoue, O., Sakai, T. & Nishida, M. 1997 Focusing shock waves generated by an accelerating projectile. *Fluid Dyn. Res.* **21**, 403–416.

Landau, L. D. & Lifshitz, E. M. 1984 *Fluid Mechanics*, 2nd edn, Vol. 6. Pergamon.

Lee, S., Lele, S. K. & Moin, P. 1993 Direct numerical simulation of isotropic turbulence interacting with a weak shock wave. *J. Fluid Mech.* **251**, 533–562.

Lele, S. K. 1992 Compact finite difference schemes with spectral-like resolution. *J. Comput. Phys.* **103**, 16–42.

Lighthill, M. J. 1953 On the energy scattered from the interaction of turbulence with sound or shock waves. *Proc. Camb. Phil. Soc.* **49**, 531–551.

McCroskey, W. J. 1995 Vortex wakes of rotorcraft. *AIAA Paper* 95–0530.

Meadows, K. R. & Caughey, D. A. 1996 The role of shock motion and deformation in the generation of shock noise. *AIAA Paper* 96–1777.

Meadows, K. R., Kumar, A. & Hussaini, M. Y. 1991 Computational study on the interaction between a vortex and a shock wave. *AIAA J.* **29**, 174–179.

Minota, T. 1993 Interactions of a shock wave with a high-speed vortex ring. *Fluid Dyn. Res.* **12**, 335–342.

Mitchell, B. E., Lele, S. K. & Moin, P. 1995 Direct computation of the sound from a compressible co-rotating vortex pair. *J. Fluid Mech.* **285**, 181–202.

Naumann, A. & Hermanns, E. 1973 On the interaction between a shock wave and a vortex field. *AGARD CP*-131, pp. 23_1-23_10.

Pao, S. P. & Salas, M. D. 1981 A numerical study of two-dimensional shock-vortex interaction. *AIAA Paper* 81–1205.

Poinsot, T. & Lele, S. K. 1992 Boundary conditions for direct simulation of compressible viscous flows. *J. Comput. Phys.* **101**, 104–129.

Ribner, H. S. 1955 Shock-turbulence interaction and the generation of noise. *NACA Rep.* 1233; see also *NACA* 3255 (1954).

Ribner, H. S. 1981 Perspectives on jet noise. *AIAA J.* **19**, 1513–1526.

Ribner, H. S. 1985 Cylindrical sound wave generated by shock-vortex interaction. *AIAA J.* **23**, 1708–1715.

Sturtevant, B & Kulkarny, V. A. 1976 The focusing of weak shock waves. *J. Fluid Mech.* **73**, 651–671.

Szumowski, A. P. & Sobieraj, G. B. 1996 Sound generation by a ring vortex-shock wave interaction. *AIAA J.* **34**, 1948–1949.

Takayama, F., Ishii, Y., Sakurai, A. & Kambe, T. 1993 Self-intensification in shock wave and vortex interaction. *Fluid Dyn. Res.* **12**, 343–348.

Tam, C. K. W. 1995 Supersonic jet noise. *Ann. Rev. Fluid Mech.* **27**, 17–43.

Taylor, G. I. 1918 On the dissipation of eddies. *Aero. Res. Commun.* 598.

Ting, L. 1974 Transmission of singularities through a shock wave and the sound generation. *Phys. Fluids* **17**, 1518–1526.

Weeks, T. M. & Dosanjh, D. S. 1967 Sound generated by shock-vortex interactions. *AIAA J.* **5**, 660–669.

Zang, T. A., Hussaini, M. Y. & Bushnell, D. M. 1984 Numerical computations of turbulence amplification in shock wave interactions. *AIAA J.* **22**, 13–21.